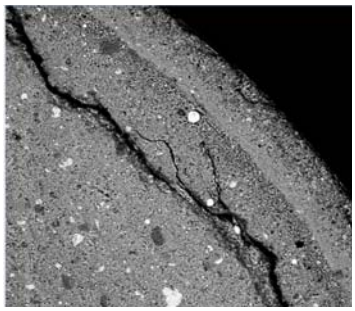

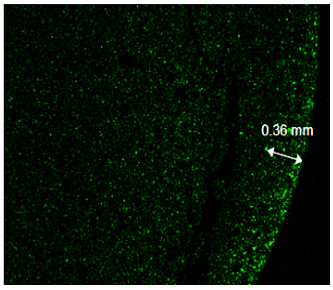

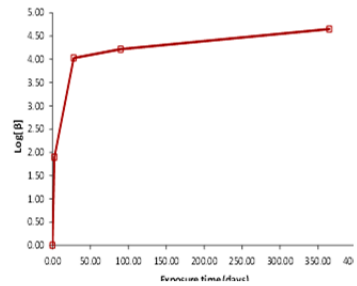

Acid Gas Interactions with Pozzolan-Amended Wellbore Cement Under Geologic Storage Conditions

September 4, 2014

Office of Fossil Energy

NRAP-TRS-III-004-2014

Disclaimer

This report was prepared as an account of work sponsored by an agency of the United States Government. Neither the United States Government nor any agency thereof, nor any of their employees, makes any warranty, express or implied, or assumes any legal liability or responsibility for the accuracy, completeness, or usefulness of any information, apparatus, product, or process disclosed, or represents that its use would not infringe privately owned rights. Reference therein to any specific commercial product, process, or service by trade name, trademark, manufacturer, or otherwise does not necessarily constitute or imply its endorsement, recommendation, or favoring by the United States Government or any agency thereof. The views and opinions of authors expressed therein do not necessarily state or reflect those of the United States Government or any agency thereof.

This report has been reviewed by the National Energy Technology Laboratory and approved for public release.

Cover Illustration: Illustrations of pozzolan-amended cement after exposure to a mixture of CO_2 and H_2S (upper left); scanning electron microscopy, back-scattered electrons (SEM-BSE) image showing CO_2 penetration (upper right); scanning electron microscopy, energy dispersive spectroscopy (SEM-EDS) mapping showing H_2S penetration (lower left); and reactive transport modeling result showing increase in permeability (lower right).

Suggested Citation: Zhang, L.; Dzombak, D. A.; Nakles, D. V. *Acid Gas Interactions with Pozzolan-Amended Wellbore Cement Under Geologic Storage Conditions*; NRAP-TRS-III-004-2014; NRAP Technical Report Series; U.S. Department of Energy, National Energy Technology Laboratory: Morgantown, WV, 2014; p 44.

An electronic version of this report can be found at:
http://www.netl.doe.gov/research/on-site-research/publications and https://edx.netl.doe.gov/nrap

Acid Gas Interactions with Pozzolan-Amended Wellbore Cement Under Geologic Storage Conditions

Liwei Zhang, David A. Dzombak, David V. Nakles

U.S. Department of Energy, National Energy Technology Laboratory, Department of Civil and Environmental Engineering, Carnegie Mellon University, 5000 Forbes Avenue, Pittsburgh, PA 15213

NRAP-TRS-III-004-2014

Level III Technical Report Series

September 4, 2014

This page intentionally left blank.

Table of Contents

ABSTRACT **1**

1. INTRODUCTION **3**
1.1 PREVIOUS STUDIES 4
1.2 RESEARCH OBJECTIVES 4

2. METHODS **6**
2.1 PREPARATION OF POZZOLAN-AMENDED CEMENT SAMPLES AND EXPERIMENTAL PROCEDURES FOR CEMENT TO ACID GAS EXPOSURE EXPERIMENTS 6
2.2 CHARACTERIZATION OF POZZOLAN-AMENDED CEMENT SAMPLES AFTER EXPOSURE EXPERIMENT 7
2.3 DETERMINATION OF CO_2 AND H_2S ALTERATION RATES OF POZZOLAN-AMENDED CEMENT 7
2.4 DEVELOPMENT OF A REACTIVE TRANSPORT MODEL TO SIMULATE INTERACTION BETWEEN POZZOLAN-AMENDED CEMENT AND CO_2+H_2S 9

3. RESULTS/OBSERVATIONS **16**
3.1 RESULTS OF OPTICAL MICROSCOPY ANALYSIS 16
3.2 RESULTS OF SEM-BSE ANALYSIS 16
3.3 RESULTS OF XRD ANALYSIS 18
3.4 RESULTS OF MICROHARDNESS TESTING 20
3.5 DETERMINATION OF CO_2 AND H_2S ALTERATION RATES BASED ON SEM-BSE AND SEM-EDS ANALYSES 21
3.6 RESULTS OF REACTIVE TRANSPORT MODELING 24

4. DISCUSSION **28**

5. CONCLUSIONS **31**

6. REFERENCES **33**

List of Figures

Figure 1: SEM-BSE image showing three distinct layers in the interface region of the 35:65 sample exposed to 1 wt% NaCl solution saturated with CO_2 and H_2S for 2.5 days. 8

Figure 2: SEM-SE image of the interface region of the 35:65 sample exposed to 1 wt% NaCl solution saturated with H_2S and CO_2 for 90 days and the EDS mapping of sulfur for the same region. 8

Figure 3: Schematic of (a) the interaction between CO_2 and pozzolan-amended cement, and (b) the interaction between H_2S and pozzolan-amended cement. 10

Figure 4: Schematic of effective vertical permeability. 14

Figure 5: Optical microscope images of unexposed 35:65 and 65:35 samples, and 35:65 and 65:35 samples exposed to a 1% NaCl brine that was in equilibrium with a supercritical mixture of 21 mol% H_2S and 79 mol% CO_2 for 28 days. 16

Figure 6: SEM-BSE images of the interface regions of (a) 35:65 and (b) 65:35 samples exposed for 2.5 days, bottom portion. 17

Figure 7: SEM-BSE images of the interior regions of unexposed 35:65 and 65:35 samples, 35:65 sample exposed to 21 mol% H_2S for 28 days, and 65:35 sample exposed to 21 mol% H_2S for 28 days. 18

Figure 8: Qualitative XRD analysis results of the interior regions of unexposed 35:65 sample (A), 35:65 sample exposed to 21 mol% H_2S for 28 days, bottom portion (B), unexposed 65:35 sample (C), and 65:35 sample exposed to 21 mol% H_2S for 28 days, bottom portion (D).. 19

Figure 9: Microhardness test results of interface and core regions of 35:65 samples (a), and interface and core regions of 65:35 samples (b). 21

Figure 10: Sulfur alteration indices of 35:65 samples exposed to 1 wt% NaCl solution saturated with CO_2 and H_2S (bottom portion) for different durations in the interface region (10-a), core region (10-b), and the entire cross-section (10-c). 22

Figure 11: Comparison between sulfur alteration indices at interior regions of 35:65 samples and 65:35 samples. Exposure periods: 0 day, 2.5 days, and 28 days. 23

Figure 12: Comparison between calcite volume % model simulation results and calcite-rich layer location data obtained from SEM-BSE images: a) 2.5 days of exposure; b) 28 days of exposure; c) 90 days of exposure. 25

Figure 13: Porosity changes from the interface region to the interior of the 35:65 sample after 2.5 days, 28 days, 90 days, 1 year, and 30 years of exposure. 26

Figure 14: Change in effective vertical permeability of the 35:65 sample from 0 to 10,950 days (30 years) of exposure. 27

Figure 15: Predicted effect of H_2S mol% in acid gas on porosity change of pozzolan-amended cement (35:65 sample). 29

List of Tables

Table 1: Summary of experimental conditions for exposure of pozzolan-amended cement to acid gas 6

Table 2: Pure-water diffusion coefficients of aqueous species. Details of how these values were obtained can be seen in Zhang (2013).....12

Table 3: Weight percentages of mineral phases in the interface region of the 65:35 samples exposed to acid gas with 21 mol% H_2S for different durations (2.5 days of exposure to 90 days of exposure) obtained from quantitative XRD analysis.....20

Table 4: Summary of locations of carbonate alteration frontier and sulfur-rich zone thickness values of 35:65 samples exposed to a saturated H_2S-CO_2 brine of 1 wt% NaCl from 2.5 days to 90 days.....21

Table 5: Rates of CO_2 and H_2S alteration (35:65 samples exposed from 2.5 days to 90 days).....23

Acronyms, Abbreviations, and Symbols

Term	Description
API	American Petroleum Institute
BET	Brunauer-Emmett-Teller
BSE	Back-scattered electron
C2S	$2CaO^{\cdot}SiO_2$, a mineral phase in cement
C3S	$3CaO^{\cdot}SiO_2$, a mineral phase in cement
C4AF	4CaO.Al2O3.Fe2O3, a mineral phase in cement
C4AH13	4CaO.Al2O3.13H2O, a mineral phase in cement
CCS	Carbon capture and storage
DOE	Department of Energy
EDS	Energy dispersive spectroscopy
GCCI	U.S. Global Climate Change Initiative
NRAP	National Risk Assessment Partnership
RP	Recommended practice
SE	Secondary electron
SEM	Scanning electron microscopy
SRZ	Sulfur-rich zone
XRD	X-ray diffraction

Acknowledgments

The work was completed as part of the National Risk Assessment Partnership (NRAP) project and was supported by the U.S. Department of Energy (DOE) through the National Energy Technology Laboratory (NETL), under Contract RES1000025, with Carnegie Mellon University. Support for this project came from the DOE Office of Fossil Energy's Crosscutting Research program. This work was funded as part of the American Recovery and Reinvestment Act of 2009. The authors wish to acknowledge Dr. Robert Romanosky (NETL Strategic Center for Coal) and Dr. Regis Conrad (DOE Office of Fossil Energy) for programmatic guidance, direction, and support.

The authors also wish to acknowledge Barbara Kutchko, Christina Lopano and Brian Strazisar at NETL, Division of Environmental Sciences, for their technical assistance regarding sample preparation and the use of analytical equipment and for providing valuable insights and suggestions on the interpretation of the experimental and modeling results and review of multiple project manuscripts. The authors also wish to thank Steve Hawthorne and David Miller at the Energy and Environmental Research Laboratory of the University of North Dakota for conducting the exposure experiments. We also would like to acknowledge Li Li and Leopold Brunet of the Department of Energy and Mineral Engineering at the Pennsylvania State University for providing the authors with the modeling software, providing instructions on its use, and offering their technical advice on the modeling of the experimental results. Lastly, the authors wish to thank Ron Ripper, Manager of the Environmental Research Laboratory of the Department of Civil and Environmental Engineering at Carnegie Mellon University, and Tom Nuhfer and Jason Wolf of the Material Science and Engineering Department for their assistance with the advanced analysis of the exposed pozzolan-amended cement samples.

This page intentionally left blank.

ABSTRACT

Emissions of acid gases (e.g., carbon dioxide (CO_2) and hydrogen sulfide (H_2S)) from the combustion of fossil fuel and the purification of natural gas, along with the high costs of separating these gases, has led to the consideration of co-storage of CO_2 and H_2S (and other acid gases) in deep saline aquifers. However, there are concerns about the safety and environmental impacts of acid gas injection, including the concern that the gas may react with wellbore cement in abandoned wells at co-storage sites, degrade and increase the permeability of the cement, and allow the acid gas to migrate from the storage reservoir. If acid gas were to migrate to subsurface sources of drinking water, surface water, or the atmosphere, it has the potential to result in risks to human health and the environment.

Previous research on reactions of pure CO_2 and brine mixtures on cement has demonstrated that in the absence of fast paths (e.g., fractures), wellbore cement will not be altered sufficiently to impact wellbore integrity on the time scales of importance to geologic carbon storage (>1,000 years) (Kutchko et al., 2007, 2009). This research investigated the interactions between pozzolan-amended wellbore cement and mixtures of CO_2 and H_2S at geologic carbon storage conditions to determine the impacts of these interactions on two wellbore cement properties that are critical to assessing potential leakage of the acid gas, i.e., porosity and permeability. The alteration of pozzolan-amended wellbore cement induced by exposure to a supercritical mixture of CO_2 and H_2S and to brine saturated with CO_2 and H_2S was examined experimentally. In addition, a reactive transport model was developed to help interpret the experimental results and to extrapolate them to the time periods of interest for a commercial-scale operation. Specific objectives of this study were: (1) to understand the response of pozzolan-amended wellbore cement to a range of mixtures of CO_2 and H_2S; (2) to quantify the alteration rates of pozzolan-amended cement with different pozzolan contents; and (3) to develop a process-based, reactive transport model to describe the geochemical and physical alterations of the pozzolan-amended wellbore cement and predict changes in effective permeability of the pozzolan-cement mixtures over time.

Two types of pozzolan-amended cement samples (35 vol% pozzolan : 65 vol% cement and 65 vol% pozzolan : 35 vol% cement, hereafter referred to as the 35:65 and 65:35 samples, respectively) were exposed to supercritical CO_2 and H_2S and to brine (1 wt% NaCl solution) saturated with CO_2 and H_2S in laboratory experiments that simulated geologic carbon storage conditions (50°C and 150 bar). Following exposure for periods of time ranging from 2.5 to 90 days, the samples were sectioned and characterized by numerous analytical methods, including scanning electron microscopy, back-scattered electrons (SEM-BSE) and scanning electron microscopy, energy dispersive spectroscopy (SEM-EDS).

Characterization of the pozzolan-cement samples exposed to a 1 wt% NaCl solution saturated with CO_2 and H_2S showed that the 35:65 samples were more resistant to CO_2 and H_2S attack. Significant alteration induced by CO_2 and H_2S only occurred in the region close to the surface of these samples after 90 days of exposure, and the rates of alteration (expressed as mm of penetration into the cement sample) were determined to be 3.3×10^{-3} mm/day (CO_2 alteration) and 4.3×10^{-3} mm/day (H_2S alteration). In contrast, for the 65:35 samples, significant alteration occurred at both the surface and the interior of the samples after 2.5 days of exposure. For the 35:65 sample, the exposure environment of CO_2/H_2S saturated brine resulted in more significant alterations of the pozzolan-cement mixture than the exposure environment of supercritical CO_2

and H_2S. In contrast, the 65:35 sample was more significantly affected by the latter exposure conditions.

The reactive transport model developed in this research predicted a significant alteration in the interface region of the 35:65 sample exposed to acid gas, indicating an increase in effective vertical permeability of 2.3×10^5 after 30 years of exposure in this interface region. Overall, this research indicates that a significant increase in permeability can occur for pozzolan-amended wellbore cement at the brine-cement interface or at the caprock-cement interface where contact occurs with brine saturated with CO_2 and H_2S. However, the effect of this increase in cement permeability on the environmental and human health risk at a storage site must be evaluated on a site-specific basis.

1. INTRODUCTION

Carbon capture and storage (CCS) is a carbon emission control strategy designed to reduce the atmospheric emissions of carbon dioxide (CO_2), a greenhouse gas that can contribute to global warming. Burning of fossil fuel is the largest anthropogenic source of CO_2, and fossil-fueled power plants account for almost half of the total CO_2 emissions from fossil fuel combustion (Rackley, 2010). CCS is an important part of the U.S. Global Climate Change Initiative (GCCI) to reduce greenhouse gas emissions (White et al., 2003). Carbon capture and storage is considered to be technically feasible at commercial scale (Gibbins and Chalmers, 2008), and the United States and Canada have initiated pilot-scale injection projects to inject CO_2 into deep saline aquifers (Hovorka, 2005; Alberta Geological Survey, 2009). Two main processes are involved in carbon capture and geologic storage. The first process, carbon capture, separates and concentrates CO_2 from flue gases; the second process, geologic storage, injects CO_2 into certain geological media to retain CO_2 in the supercritical phase or dissolved in formation water to prevent its return to the atmosphere.

Co-storage of hydrogen sulfide (H_2S) with CO_2 is one option being considered to reduce environmental impacts associated with the release of H_2S or to reduce the costs associated with the separation and handling of H_2S. Large amounts of CO_2 are produced during the use of fossil fuels. Sulfur compounds, also released during the use of fossil fuels at stationary plants, usually must be captured and disposed of, as required by environmental regulations. Many systems that capture CO_2 also capture sulfur compounds, so co-storage avoids the costs associated with separation and additional processing of the separated sulfur compounds. Similarly, the purification of “sour” natural gas (natural gas that has significant amounts of H_2S) can be accompanied by co-capture of the CO_2 along with the H_2S. The economics and technical feasibility of the co-storage of CO_2 and H_2S is currently under investigation. For example, mixing CO_2 with H_2S can result in an increase of supercritical pressure and thus result in an additional cost to raise the operation pressure during the injection process (Carroll, 2010). On the other hand, this cost may be offset by eliminating the cost to separate H_2S from CO_2. Furthermore, the solubility of H_2S in saline water is higher than that of CO_2 under subsurface conditions (Kutchko et al., 2011), which means that a saline aquifer may have enough capacity to store both CO_2 and H_2S at a given site.

Concurrent with the investigation of the economics and technical feasibility of the co-storage of CO_2 and H_2S, the environmental and safety risks associated with CO_2 and H_2S co-storage are also being assessed. One of the primary risks of interest is the degradation of wellbore cement integrity in active and abandoned wells, which could lead to leakage of CO_2 and H_2S from the storage reservoir. Previous studies have focused on wellbore cement integrity under carbon storage conditions, with CO_2 as the only injected gas (Barlet-Gouédard et al., 2007; Carey et al., 2007; Kutchko et al., 2007; Brandvoll et al., 2009; Huet et al., 2010; Fabbri et al., 2012; Wertz et al., 2013). There has been some investigation of the interaction of a mixture of CO_2 and H_2S with wellbore cement (Jacquemet et al., 2008; Kutchko et al., 2011; Jacquemet et al., 2012), but no studies have been conducted for CO_2-H_2S interaction with pozzolan-amended cement (a widely-used type of wellbore cement with pozzolan, a siliceous and aluminous material, as an additive).

1.1 PREVIOUS STUDIES

Wellbore cement integrity under geologic carbon storage conditions has been the subject of investigation for the past decade. Most research has focused on interaction between wellbore cement and CO_2 under geologic carbon storage conditions (Duguid et al., 2004; Duguid et al., 2005; Kutchko et al., 2007; Barlet-Gouédard et al., 2009; Carey et al., 2010; Newell and Carey, 2013; Mason et al., 2013).

A brief review of previous studies investigating the interaction between wellbore cement and mixtures of CO_2 and H_2S under geologic acid gas storage conditions reveals that the earliest lab-scale study on the interaction between wellbore cement and acid gas was conducted by Jacquemet et al. (2008) at Université Nancy in France. The authors studied three experimental scenarios: a brine with dissolved H_2S-CO_2; a dry H_2S-CO_2 supercritical phase; and a two-phase fluid consisting of a H_2S-CO_2 containing brine with a H_2S-CO_2 supercritical phase. The H_2S reactivity with cement was limited since it only transformed ferrites and hydration products of ferrites (minor phases in cement) by sulfidation, and the only product of sulfidation they observed was pyrite (Jacquemet et al., 2008). Different from the results obtained by Jacquemet et al. (2008), Kutchko et al. (2011) observed formation of abundant ettringite and other amorphous sulfur-rich particles at core regions of hydrated class H cement samples exposed to both supercritical CO_2-H_2S (H_2S mol% = 21%) and brine saturated with CO_2 and H_2S for 28 days. The reason Jacquemet et al. (2008) did not observe the formation of ettringite is that they used fine cement powders in the exposure experiment, which results in low pH pore water in the cement matrix. As ettringite cannot exist at low pH conditions, all ettringite was dissolved in the samples of Jacquemet et al. (2008). Although Kutchko et al. (2011) observed the formation of ettringite, which has the potential to cause strength loss and degradation of the mechanical integrity of the cement, mechanical damage induced by ettringite formation was not observed in the exposed cement samples. The authors concluded that the mineralogical changes and alteration front were controlled by buffering of local pore water pH (Kutchko et al., 2011).

In summary, some studies have investigated the mineralogical changes of wellbore cement exposed to CO_2 and H_2S under geologic acid gas storage conditions, but studies are needed to provide more comprehensive information about interaction between wellbore cement and acid gas interaction under different scenarios (e.g., a range of H_2S concentrations, cement compositions, or exposure conditions). The rate of cement alteration under these scenarios needs to be quantified and incorporated into a model that predicts changes in the cement properties over time. Ultimately, this model will be part of an integrated modeling effort to assess site-specific risks of acid gas leakage at co-storage sites.

1.2 RESEARCH OBJECTIVES

The overall goal of the research was to improve the understanding of the permeability change in pozzolan-amended wellbore cement induced by CO_2 and H_2S attack under co-storage conditions and to develop a model to predict these changes over the lifetime of a typical geologic carbon storage site. Information about the permeability change of pozzolan-amended wellbore cement under geologic carbon storage conditions can be incorporated into integrated risk assessment models. Pozzolan-amended wellbore cement was chosen for this study, because pozzolan-amended Portland cement is one of the most common types of cement systems used for well sealing in oil and gas fields (American Petroleum Institute, 1991). Among the many types of available pozzolanic materials, type F fly ash, the most common pozzolan used in well cement

(minimum 70 wt% of SiO_2, Al_2O_3 and Fe_2O_3 and maximum 20 wt% of CaO), was chosen as the pozzolanic material used in Kutchko et al. (2009).

The overall goal was achieved by addressing the following three objectives: (1) understand the response of pozzolan-amended wellbore cement to CO_2 and H_2S attack; (2) quantify CO_2 and H_2S alteration rates of pozzolan-amended cement with different pozzolan contents; and (3) develop a process-based, reactive transport model capable of describing the interactions of a CO_2-H_2S-brine mixture with pozzolan-amended wellbore cement and predicting changes in effective permeability of wellbore cement over time.

To achieve the first and second objectives, laboratory experiments were conducted that exposed two pozzolan-amended cement mixtures, containing 35% and 65% pozzolan, to acid gases containing from 1% to 40% H_2S, for periods ranging from 2.5 to 90 days. Exposure to the acid gas in its supercritical state as well as to brines in equilibrium with the acid gas was investigated at conditions representative of geologic carbon storage (i.e., 50°C and 150 bar). The exposed cement samples were sectioned and analyzed to determine the geochemical reactions that had occurred, the rate of these reactions, and the extent of penetration of the reactions into the cement.

The third objective was achieved by developing a conceptual model to describe chemical alterations of pozzolan-amended cement under geologic acid gas storage conditions and using a reactive transport model CrunchFlow (Steefel, 2009; Li et al., 2010), to describe and help interpret the rates of alterations based on the conceptual model. This reactive transport model is capable of predicting the penetration of CO_2 and H_2S into the pozzolan-amended wellbore cement, and relating these chemical alterations to changes in porosity and permeability.

2. METHODS

2.1 PREPARATION OF POZZOLAN-AMENDED CEMENT SAMPLES AND EXPERIMENTAL PROCEDURES FOR CEMENT TO ACID GAS EXPOSURE EXPERIMENTS

Two types of pozzolan-amended Portland cement samples were prepared: 35% by volume pozzolan and 65% by volume cement (35:65 sample); and 65% by volume pozzolan and 35% by volume cement (65:35 sample). The cement was mixed with pozzolan according to American Petroleum Institute (API) Recommended Practice (RP) 10B (section 17.4) (American Petroleum Institute, 1997). The slurry densities (1.74 g/cm^3 for 35:65 sample and 1.64 g/cm^3 for 65:35 sample) were chosen to represent an average slurry density of field samples. The water:cement ratio for the 35:65 sample was 0.51, and the water : cement ratio for the 65:35 sample was 0.56. Samples were submerged in a 1 wt% NaCl solution as previously described in Kutchko et al. (2007) for curing. The cement was allowed to cure for a total of 28 days at a temperature of 50°C and a water pressure of 15 MPa to simulate a geologic carbon storage depth of approximately 1,300 m.

After curing, the pozzolan-amended cement samples (12 mm inner diameter × 60 mm height) were placed in glass vials with half of each vial filled with 1% NaCl solution. A total of 12 individual vials were placed in a rack (three individual vials placed on four levels), which was placed inside a high-pressure vessel made of stainless steel. Samples were exposed to H_2S/CO_2 mixtures with an H_2S concentration ranging from 1% to 40% for different exposure periods (2.5 to 90 days). A summary of sample exposure conditions is shown in Table 1. Details of sample exposure procedures are available in Hawthorne et al. (2011) and Zhang (2013).

Table 1: Summary of experimental conditions for exposure of pozzolan-amended cement to acid gas

Sample Description	Exposure Scenarios		Reaction Duration, days	Pressure, psi	Temperature, °C
	Top Portion of Sample	Bottom Portion of Sample			
35 Pozzolan : 65 Cement	Exposed to supercritical $H_2S + CO_2$ (1 mol%, 21 mol% and 40 mol% H_2S), no brine	Exposed to 1 wt% NaCl brine exposed to supercritical CO_2 and H_2S (1 mol%, 21 mol% and 40 mol% H_2S)	2.5, 9, 28, and 90	2,200 (150 bar)	50
65 Pozzolan : 35 Cement	Exposed to supercritical $H_2S + CO_2$ (1 mol%, 21 mol% and 40 mol% H_2S), no brine	Exposed to 1 wt% NaCl brine exposed to supercritical CO_2 and H_2S (1 mol%, 21 mol% and 40 mol% H_2S)	2.5, 9, 28, and 90	2,200 (150 bar)	50

2.2 CHARACTERIZATION OF POZZOLAN-AMENDED CEMENT SAMPLES AFTER EXPOSURE EXPERIMENT

As listed below, optical microscopy, scanning electron microscopy, back-scattered electrons (SEM-BSE), scanning electron microscopy, energy dispersive spectroscopy (SEM-EDS), X-ray diffraction (XRD), microhardness testing, and Brunauer-Emmett-Teller (BET) testing were applied to examine different characteristics of the pozzolan-amended cement samples after exposure to acid gas (Zhang, 2013):

- The optical microscopy analysis was applied to observe meso-scale changes in appearance as a result of mineral phase changes
- SEM-BSE analysis was applied to distinguish micro-scale differences in different mineral phases
- SEM-EDS analysis was applied to evaluate the change of elemental content (e.g., total Ca wt% and total S wt%) in the solid phase of the samples
- XRD analysis was applied to identify the formation of minerals in the cement
- Microhardness testing was applied to evaluate the change of mechanical strength of the samples
- BET testing was applied to evaluate the change of porosity of the samples

2.3 DETERMINATION OF CO_2 AND H_2S ALTERATION RATES OF POZZOLAN-AMENDED CEMENT

SEM-BSE imaging was used to evaluate the CO_2 alteration rate, because the evidence of CO_2 attack could be seen clearly delineated using SEM-BSE observations (Figure 1). In this work, the maximum distance between the frontier of the $CaCO_3$-rich layer (the interface between Layer B and Layer C in Figure 1) and the surface of the sample was defined as the location of carbon alteration frontier, and the location of carbon alteration frontier was used as the criterion to evaluate the rate of CO_2 attack. The location of carbon alteration frontier was obtained by measuring the distance between the surface and the $CaCO_3$-rich layer frontier of the sample in the SEM-BSE image. To assure the accuracy of the location of carbon alteration frontier, four different measurements of the location of the carbon alteration frontier were made for every sample and the average value of the four measurements was used as the final location (details of the measurements can be seen in Zhang, 2013).

Based on a literature search and with consideration of the available experimental data, the concentration change of elemental sulfur was chosen to represent the alteration rates of samples undergoing H_2S attack. The alteration rate is described by two different parameters: sulfur-rich zone thickness (obtained from SEM-EDS mapping) and sulfur alteration index (obtained from SEM-EDS point analysis). Similar to the location of carbon alteration frontier, sulfur-rich zone thickness is defined as the maximum distance between the surface of the sample and the frontier of the sulfur-rich zone in the interface region. A schematic of sulfur-rich zone thickness can be seen in Figure 2. To determine sulfur-rich zone thickness, SEM-EDS mapping was applied to obtain sulfur distribution maps of sample cross-sections with the use of the INCA X-ray microanalysis system (Oxford Instruments, Abingdon, UK) associated with the Quanta 600 SEM. To assure the accuracy of sulfur-rich zone thickness, the sulfur-rich zone thickness values were measured at four different locations for every sample and the average value was used as the final thickness (details of the measurements can be seen in Zhang, 2013).

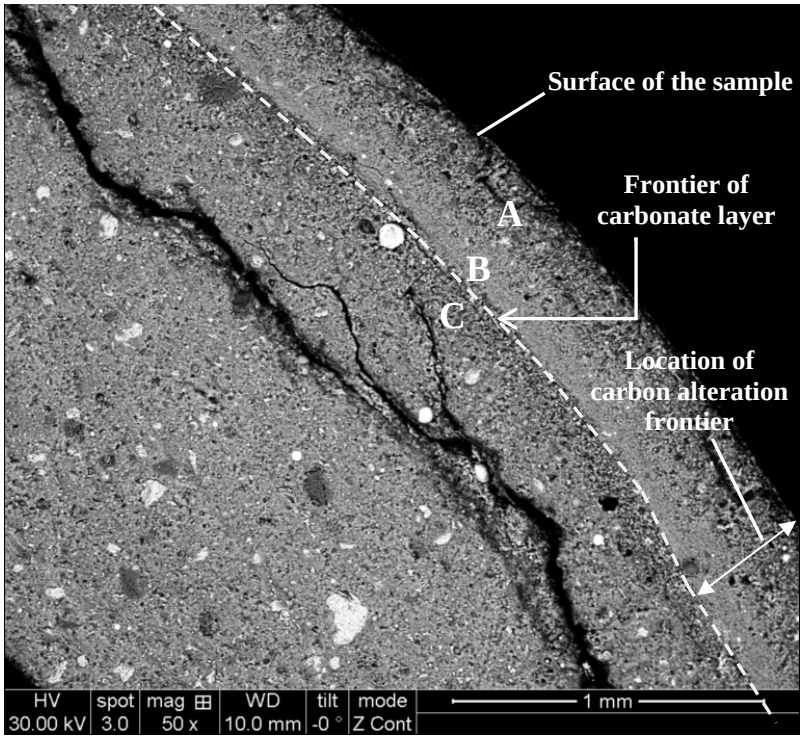

Figure 1: SEM-BSE image showing three distinct layers in the interface region of the 35:65 sample exposed to 1 wt% NaCl solution saturated with CO_2 and H_2S (bottom portion) for 2.5 days. The layer closest to the surface of the sample (Layer A) was a porous layer which was rich in Si-bearing minerals. A bright and dense $CaCO_3$-rich layer (Layer B) could be observed next to Layer A. Layer C was a region in which some of the Ca-bearing minerals were dissolved. The location of carbon alteration frontier is defined as the maximum distance between the surface of the sample and the frontier of the $CaCO_3$-rich layer.

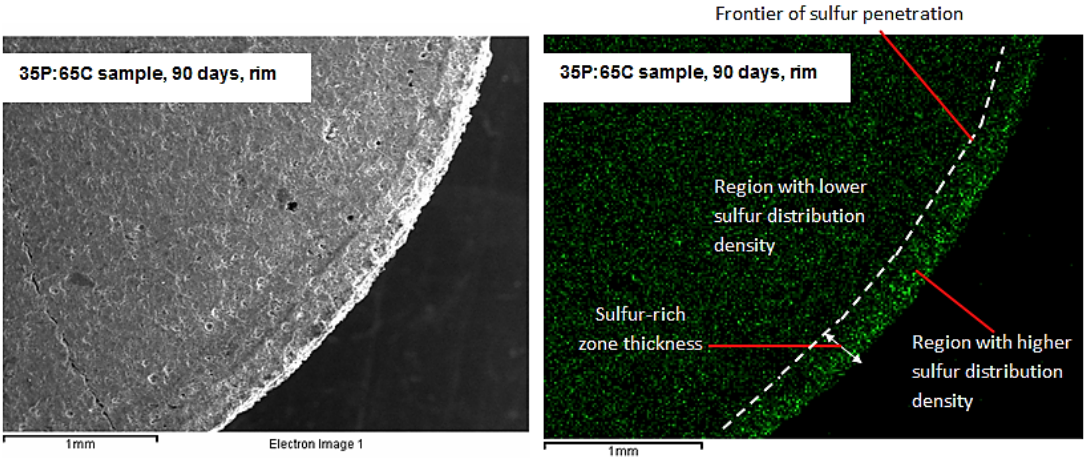

Figure 2: SEM-SE image of the interface region of the 35:65 sample exposed to 1 wt% NaCl solution saturated with H_2S and CO_2 (bottom portion) for 90 days (left) and the EDS mapping of sulfur for the same region (right). The frontier of sulfur penetration can be observed clearly in the image at right. Sulfur-rich zone thickness is the maximum distance between the surface of the sample and the frontier of the sulfur penetration zone.

The sulfur alteration index, which was developed as part of this research effort, uses the difference between the measured sulfur wt % in the exposed sample and the background sulfur wt % in the unexposed sample to evaluate the level of alteration caused by H_2S attack. All sulfur wt % values were obtained from SEM-EDS point analysis. Details of SEM-EDS point analysis are presented in Zhang (2013).

The sulfur alteration index is used to overcome the limitations of using sulfur-rich zone thickness to evaluate sulfur alteration level. These limitations include: 1) difficulty in observing the sulfur penetration boundary to determine the sulfur-rich zone thickness; and 2) samples with the same sulfur-rich zone thickness can have different sulfur contents, which means samples with the same sulfur-rich zone thickness can have different levels of sulfur alteration.

The sulfur alteration index (dimensionless) is defined as:

$$I = \frac{1}{N}\sum_{i=1}^{N}\left(\frac{S_i - S_b}{S_i}\right) \tag{1}$$

where I is the sulfur alteration index of the sample, N is the total number of points analyzed by SEM-EDS, S_i is the sulfur content at point i (total S wt% in solid), and S_b is the average background sulfur content obtained from the unexposed samples. For the unexposed 35:65 sample, S_b is equal to 0.59% (a detailed description of how the background value was obtained is provided in Zhang, 2013). If S_i is smaller than S_b, the term $(S_i - S_b)/S_i$ is set to zero. More information about the sulfur alteration index can be found in Zhang et al. (2014).

To determine the sulfur alteration index, the sulfur content in both interface and interior regions of the exposed samples were obtained by SEM-EDS point analysis with the use of the INCA system. For every sample, 20 spots were analyzed in both the interface region (the surface to ~ 1 mm away from the surface) and the interior region of the sample to assure the representativeness of the measurements.

In this study, the locations of the carbon alteration frontier and the values of sulfur-rich zone thickness of the bottom portion of 35:65 samples exposed to a mixture of acid gas (21 mol% H_2S and 79 mol% CO_2) for 2.5, 9, 28, and 90 days were obtained. The sulfur alteration index values for the same samples in both interface and interior regions were also obtained. All those values were compiled and used to quantify the rates of CO_2 and H_2S alteration.

2.4 DEVELOPMENT OF A REACTIVE TRANSPORT MODEL TO SIMULATE INTERACTION BETWEEN POZZOLAN-AMENDED CEMENT AND CO_2+H_2S

2.4.1 The conceptual model of the interaction between pozzolan-amended cement and CO_2+H_2S

The interaction between CO_2 and H_2S and wellbore cement under typical co-storage conditions is complicated, and involves dissolution of key cementitious phases (portlandite and amorphous calcium-silicate-hydrate (C-S-H)), precipitation and dissolution of carbonate species (calcite), formation of sulfur-containing species (ettringite and pyrite), and gradual change of pH from the surface to the interior of the cement. Figures 3(a) and 3(b) show schematics of the interaction

between CO_2 and pozzolan-amended cement and between H_2S and pozzolan-amended cement, respectively.

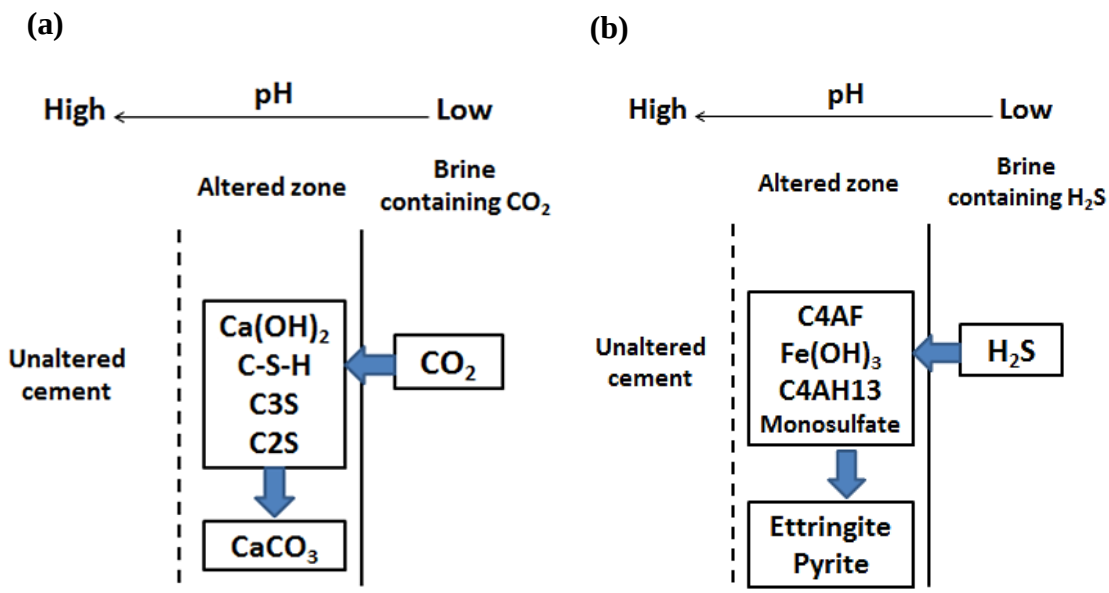

Figure 3: Schematic of (a) the interaction between CO_2 and pozzolan-amended cement, and (b) the interaction between H_2S and pozzolan-amended cement. Abbreviations of minerals: C-S-H = amorphous calcium-silicate-hydrate, C3S = $3CaO{\cdot}SiO_2$, C2S = $2CaO{\cdot}SiO_2$, C4AF = $4CaO{\cdot}Al_2O_3{\cdot}Fe_2O_3$, and C4AH13 = $4CaO{\cdot}Al_2O_3{\cdot}13H_2O$.

2.4.2 Development of the reactive transport model

Based on the conceptual model developed in Section 2.4.1, a reactive transport model that simulates the interaction between pozzolan-amended cement and CO_2-H_2S was developed. The reactive transport model is able to quantitatively predict the volume percentage change of minerals as a result of acid gas interaction with cement and the change of porosity as a result of these changes in volume. The multicomponent reactive transport modeling code CrunchFlow (Steefel, 2009; Li et al., 2010) was used to develop the model. The mass conservation equation is the fundamental equation used in CrunchFlow. The expression of mass conservation equation is (revised from Steefel and Lasaga, 1994):

$$\frac{d(\emptyset C_i)}{dt} = \frac{d}{dx}\left(\emptyset D_{ie}\frac{dC_i}{dx}\right) - \frac{d}{dx}(\emptyset u C_i) \pm \sum_{i=1}^{N} v_{ir} R_{ir} \qquad (2)$$

Diffusion term **Advection term** **Reaction term**

where, $\emptyset$ is the porosity of the porous media (unitless), C_i is the concentration of species i (mol/m^3), D_{ie} is the effective diffusion coefficient of species i (m^2/s), u is flow velocity (m/s), R_{ir} is the rth reaction rate that can produce or consume species i (mol/m^3·s) and v_{ir} is stoichiometric

number of species i in the rth reaction (unitless). It is important to note that since the modeling effort is for a static, or no-flow condition, the advection term is set equal to 0 (i.e., $u = 0$).

Given the values of the three parameters ($\emptyset$, D_e and R) in Equation 2, Crunchflow can solve the mass conservation equation and generate concentration profiles of all aqueous species as a function of time. The details for calculating these parameters are described below.

$\emptyset$—Porosity of cement

The porosity of the cement matrix can be expressed as a function of the volume fractions of all mineral phases (Xu et al., 2004):

$$\phi(t) = 1 - \sum_{i=1}^{m} fr_i(t) - fr_n \tag{3}$$

where, $\emptyset$(t) is the porosity of cement at time t, $fr_i(t)$ is the volume fraction of reactive mineral phase i at time t and fr_n is the volume fraction of all inert mineral phases in the cement. CrunchFlow calculates the volume fractions of all reactive mineral phases, based on the dissolution/precipitation reactions that occur on the surfaces of reactive mineral phases.

D_{ie}—Effective diffusion coefficient of species *i*

To calculate effective diffusion coefficients of the species, the corresponding diffusion coefficients of species in the pure water were obtained. Pure-water diffusion coefficients of charge-neutral species (e.g., CO_2 and H_2S) were calculated by the Wilke—Chang equation (Wilke and Chang, 1955), and pure-water diffusion coefficients of charged species were obtained from the literature. Table 2 summarizes the pure-water molecular diffusion coefficients of all aqueous species considered in the modeling.

Following the input of the pure-water diffusion coefficients of all species into CrunchFlow, the program converts pure-water diffusion coefficients into effective diffusion coefficients (D_e) in porous media. CrunchFlow allows several approaches to be used for the calculation of D_e. In this work, D_e (m^2s^{-1}) was calculated as a function of pure-water diffusion coefficient (D_0), the inverse of the tortuosity (1/tortuosity,T), and porosity (θ) (Marty et al., 2009):

$$D_e = D_0 T \theta \tag{4}$$

It is important to note that in this work, tortuosity was defined as the length of the pathway divided by the shortest distance between the ends of the pathway. That is to say, tortuosity is always higher than 1 and T in Equation 4 is always lower than 1 in porous media.

R_{ir}—Reaction rate of species *i* in rth reaction

R_{ir} is the overall reaction rate for a specific reaction r that can produce or consume species i. CrunchFlow assumes that the reactions between ion and mineral involving adsorption and desorption of ions at mineral surfaces are the rate-limiting reactions, while reactions involving

aqueous species only (except for oxidation—reduction reactions) are assumed to be rapid reactions. As a result, if R_{ir} is a reaction rate associated with a reaction having a mineral as a reactant, the rate will be calculated based on mineral dissolution/precipitation rate law as discussed below. The simplified expression of the mineral dissolution/precipitation rate law can be written as (Steefel, 2009):

Table 2: Pure-water diffusion coefficients of aqueous species. Details of how these values were obtained can be seen in Zhang (2013)

Species	D_0 (10^{-5} cm^2/s, T = 298K)	D_0 (10^{-5} cm^2/s, T = 323K)
H^+	9.310	16.790
Ca^{2+}	0.790	1.420
OH^-	5.280	9.520
SO_4^{2-}	1.060	1.910
Fe^{2+}	0.670	1.210
Fe^{3+}	0.700	1.230
Na^+	1.330	2.340
Cl^-	2.030	3.570
HS^-	1.730	3.080
S^{2-}	1.350	2.410
HCO_3^-	1.185	2.110
CO_3^{2-}	0.923	1.650
Al^{3+}	0.541	0.965
CO_2	Not calculated	3.770
H_2S	Not calculated	3.840

$$R_{ir} = A\left(\sum_{l=1}^{M} k_l\left(\prod_{i=1}^{N} a_i^{p_i}\right)\left(1 - \frac{Q}{K_{eq}}\right)\right) \quad (5)$$

where, A is the specific surface area (m^2/m^3) of the mineral involved in the reaction, k_l is the lth parallel reaction rate constant (mol/m^2s) that contributes to the dissolution/precipitation of the mineral, $\prod_{i=1}^{N} a_i^{p_i}$ describes the effects of various ions in solution on the dissolution or precipitation rate of parallel reaction l (k_l), Q is ion activity product (e.g., for reaction aA + bB

== cC + dD, where Q is equal to $\frac{[C]^c[D]^d}{[A]^a[B]^b}$), and K_{eq} is equilibrium constant of the reaction. The ratio of Q to K_{eq} determines the direction of the reaction. For example, given calcite dissolution reaction:

$$CaCO_3 + H^+ == Ca^{2+} + HCO_3^- \tag{6}$$

If Q is higher than K_{eq}, then the system is supersaturated with Ca^{2+} and HCO_3^-, and the reaction will become the calcite precipitation reaction.

It is important to note that there are uncertainties associated with Equation 5, and the uncertainties mainly stem from the lack of reliable information on the values of mineral reactive surface areas and their variation with time, as well as the variation of reaction rate constants over a large span of Gibbs free energy of reactions (Gherardi et al., 2012). As a result, the values of A and k_ls in Equation 5 that were obtained from literature may not fit a particular system of interest. In this work, a data fitting process was conducted to obtain appropriate k_l values, and some k_l values were changed from the initial values found in the literature. Details of the fitting processes of *k* values can be found in Appendix D of Liwei Zhang's dissertation (Zhang, 2013).

CrunchFlow requires input of all chemical reactions (e.g., formula of reactions, equilibrium constants of reactions, and reaction rate constants) involved in cement—acid gas interactions. A complete list of reactions involved can be seen in Zhang (2013).

2.4.3 Model outputs and validation of model outputs

The 1-D reactive transport model developed using CrunchFlow is able to produce calcite volume percentage, total Ca and S weight percentages in the solid phase, and local porosity at every block (block size is 0.01 mm and there are 600 blocks in the entire cement sample modeling domain) from the surface to the interior of pozzolan-amended cement sample. The change in local porosity can be correlated with the change in local permeability using a power law relationship (Ghabezloo et al., 2009; Brunet et al., 2013):

$$\frac{perm_{i,t}}{perm_{i,0}} = \left(\frac{\emptyset_{i,t}}{\emptyset_{i,0}}\right)^n \tag{7}$$

where, $perm_{i,t}$ is the local permeability value in the block *i* at time *t*; $perm_{i,0}$ is the initial permeability; $\emptyset_{i,t}$ is the porosity value in the block *i* at time *t*; $\emptyset_{i,0}$ is the initial porosity; and *n* is estimated to be 11 (Brunet et al., 2013). A schematic of vertical effective permeability is presented in Figure 4.

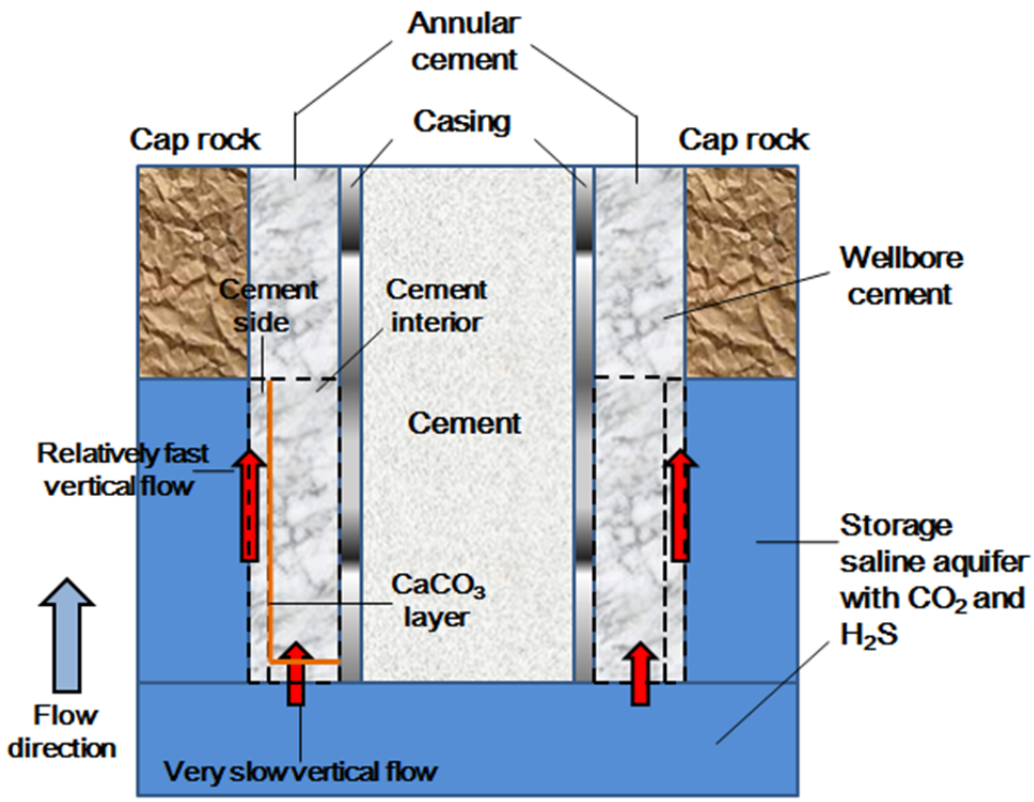

Figure 4: Schematic of effective vertical permeability.

The change in effective permeability compared with the original permeability (β) is quantified by the following equation:

$$\beta_t = \frac{perm_{e,t}}{perm_{e,0}} \tag{8}$$

where, $perm_{e,t}$ is the effective permeability at time t, and $perm_{e,0}$ is the effective permeability at time 0. It is important to note that $perm_{e,0} = perm_{i,0}$, $i = 1, 2, \ldots, n$.

To enable comparison with data from the exposure experiments (exposure times were 2.5, 9, 28 and 90 days), model simulation results for 2.5, 28 and 90 days of exposure were obtained. Predictions of effective permeability of samples after 30 years were also simulated as a means to evaluate the potential for acid gas leakage after longer periods of exposure.

To assure the reliability of model outputs, the predicted calcite vol%, total Ca wt% and total S wt% produced by the model were validated by comparison with SEM-BSE images and SEM-EDS data of the corresponding cement samples, which were analyzed after exposure to CO_2 and H_2S. SEM-BSE images provided the location of a calcite-rich layer, which was used to validate calcite vol% results; SEM-EDS analyses provided data for total Ca wt% and total S wt% in the solid phase from the surface to the interior of the sample. These data were used to validate the

predicted total Ca wt% and total S wt% results from the model simulations. Refer to Zhang (2013) for the details of SEM-BSE imaging and SEM-EDS analyses.

3. RESULTS/OBSERVATIONS

3.1 RESULTS OF OPTICAL MICROSCOPY ANALYSIS

Figure 5 shows optical microscope images of unexposed 35:65 and 65:35 samples, as well as 35:65 and 65:35 samples after 28 days of exposure. All samples were exposed to a 1 wt% NaCl brine saturated with H_2S and CO_2 (the brine was in equilibrium with a supercritical mixture of 21 mol % H_2S and 79 mol % CO_2.). The cross-sections of unexposed 35:65 and 65:35 samples look similar to each other, but after 28 days of exposure, the images of the cross-sections of the 35:65 and 65:35 samples are noticeably different. These differences can be attributed to the occurrence of CO_2 and H_2S alteration in both the interface and interior regions of the 65:35 sample. In contrast, the CO_2 and H_2S alteration for the 35:65 sample was only visible in the rim region, and no alteration in the interior region was observed in the optical microscope image.

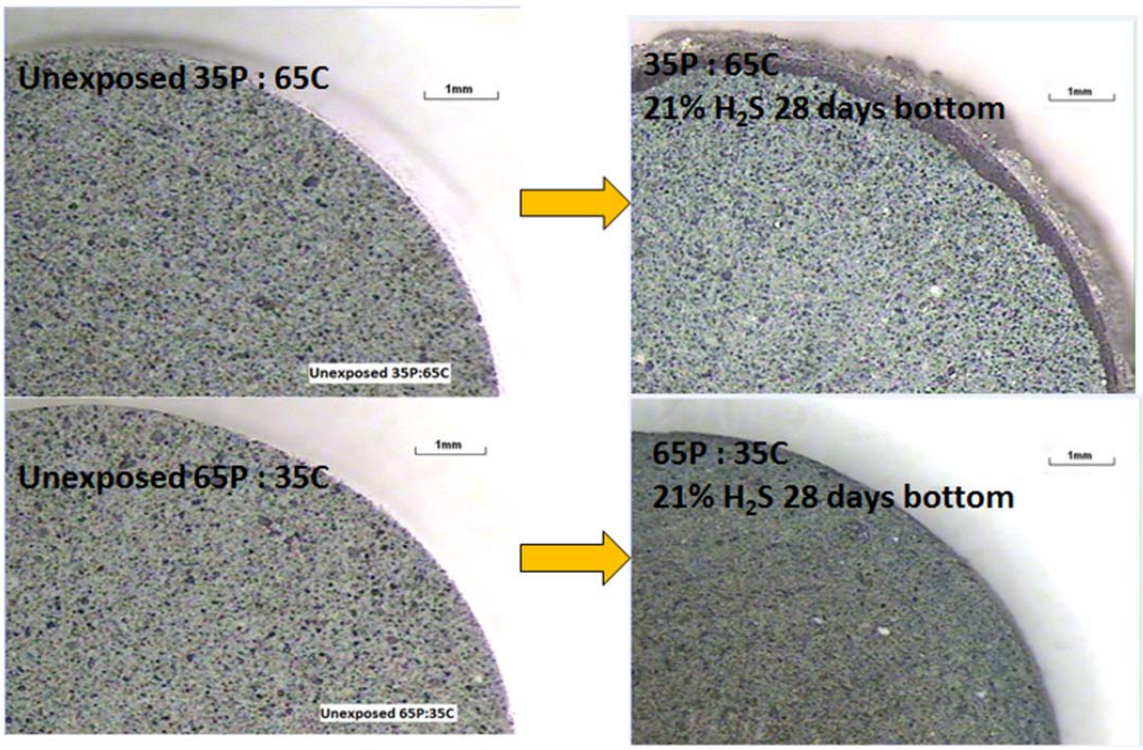

Figure 5: Optical microscope images of unexposed 35:65 and 65:35 samples, and 35:65 and 65:35 samples exposed to a 1% NaCl brine that was in equilibrium with a supercritical mixture of 21 mol% H_2S and 79 mol% CO_2 for 28 days (i.e., bottom portion of the sample).

3.2 RESULTS OF SEM-BSE ANALYSIS

Figure 6 shows the SEM-BSE images of the interface regions of 35:65 and 65:35 samples exposed to brine that was in equilibrium with a supercritical mixture of 21 mol% H_2S and 79 mol% CO_2 for 2.5 days (bottom portion). For the 35:65 sample, three distinct altered layers can be observed in the interface region, as shown in Figure 6(a): porous $CaCO_3$-depleted layer,

$CaCO_3$-rich layer, and calcium-bearing mineral dissolution layer. For the 65:35 sample, no distinct altered zones were observed in the interface region, as shown in Figure 6(b).

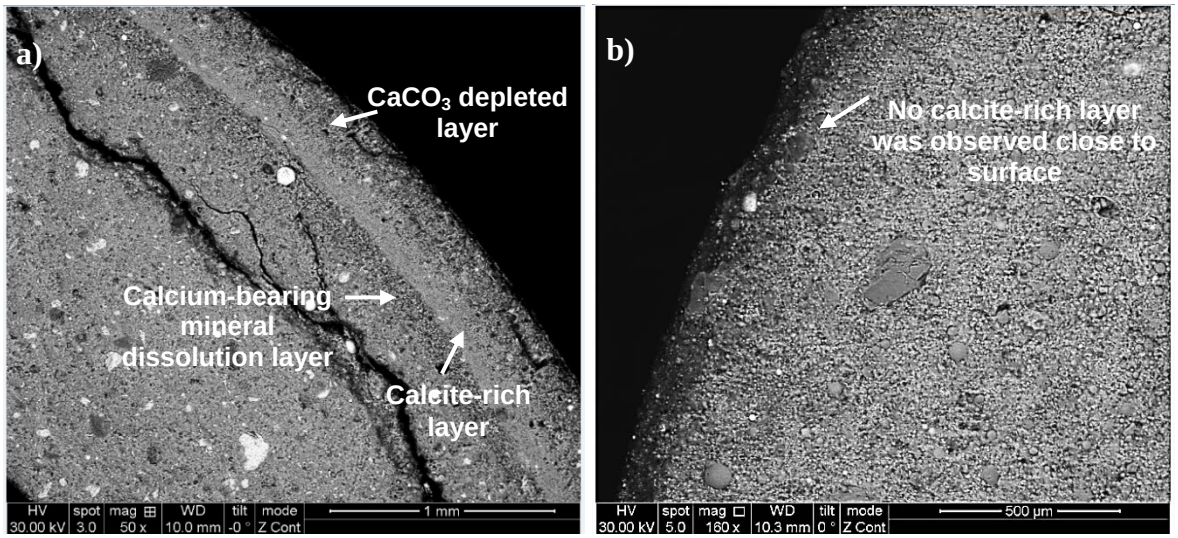

Figure 6: SEM-BSE images of the interface regions of (a) 35:65 and (b) 65:35 samples exposed for 2.5 days, bottom portion (e.g., exposed to brine that was in equilibrium with a supercritical mixture of 21 mol% H_2S and 79 mol% CO_2).

Figure 7 shows the SEM-BSE images of the interior regions of unexposed 35:65 sample, unexposed 65:35 sample, 35:65 sample exposed for 28 days (bottom portion) and 65:35 sample exposed for 28 days (bottom portion). It can be seen that the number of unhydrated cement grains (grains marked by “U”) at the interior region of the 35:65 sample after 28 days of exposure decreased somewhat, but the C-S-H binding phase in the interior region remained unaltered. In contrast, the interior region of the 65:35 sample showed a complete loss of unhydrated cement grains after 28 days of exposure and the C-S-H binding phase was significantly altered as well.

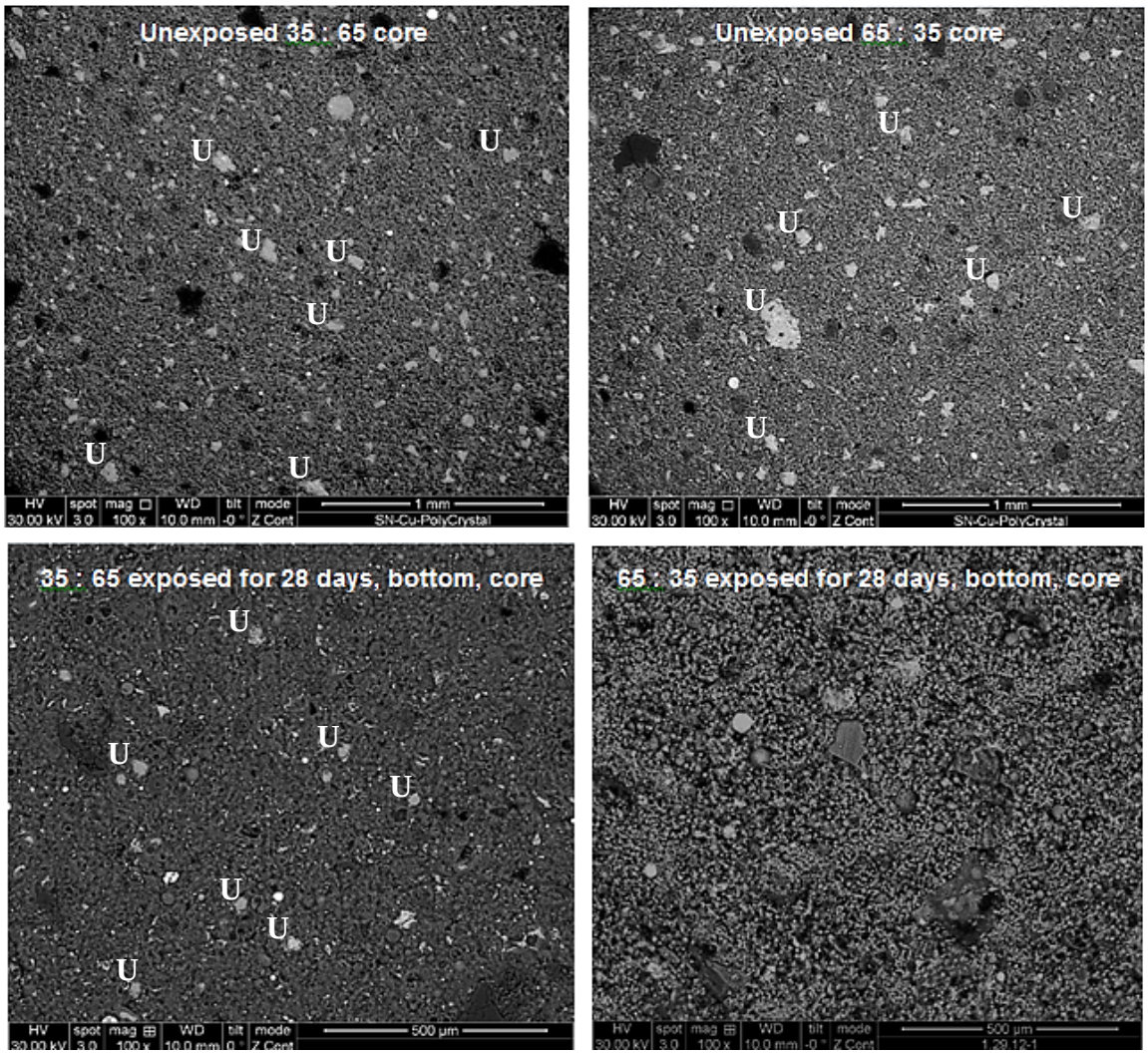

Figure 7: SEM-BSE images of the interior regions of unexposed 35:65 and 65:35 samples, 35:65 sample exposed to 21 mol% H_2S for 28 days (bottom portion), and 65:35 sample exposed to 21 mol% H_2S for 28 days (bottom portion).

3.3 RESULTS OF XRD ANALYSIS

Figure 8 shows the qualitative XRD analysis results for the interior regions of the unexposed 35:65 sample, the 35:65 sample exposed to 21 mol% H_2S for 28 days (bottom portion), the unexposed 65:35 sample and the 65:35 sample exposed to 21 mol% H_2S for 28 days (bottom portion). Compared with the XRD spectrum of the unexposed sample, the XRD pattern of the interior region of the 35:65 sample exposed for 28 days did not show peaks of aragonite and calcite, which implies that the interior region of 35:65 sample exposed for 28 days is not altered significantly by CO_2. However, for the 65:35 sample, the peaks of carbonate species (calcite and aragonite) were seen clearly in the XRD spectrum of the interior region after 28 days of exposure, which suggests that CO_2-induced alteration penetrates to the interior region of the 65:35 sample after 28 days of exposure.

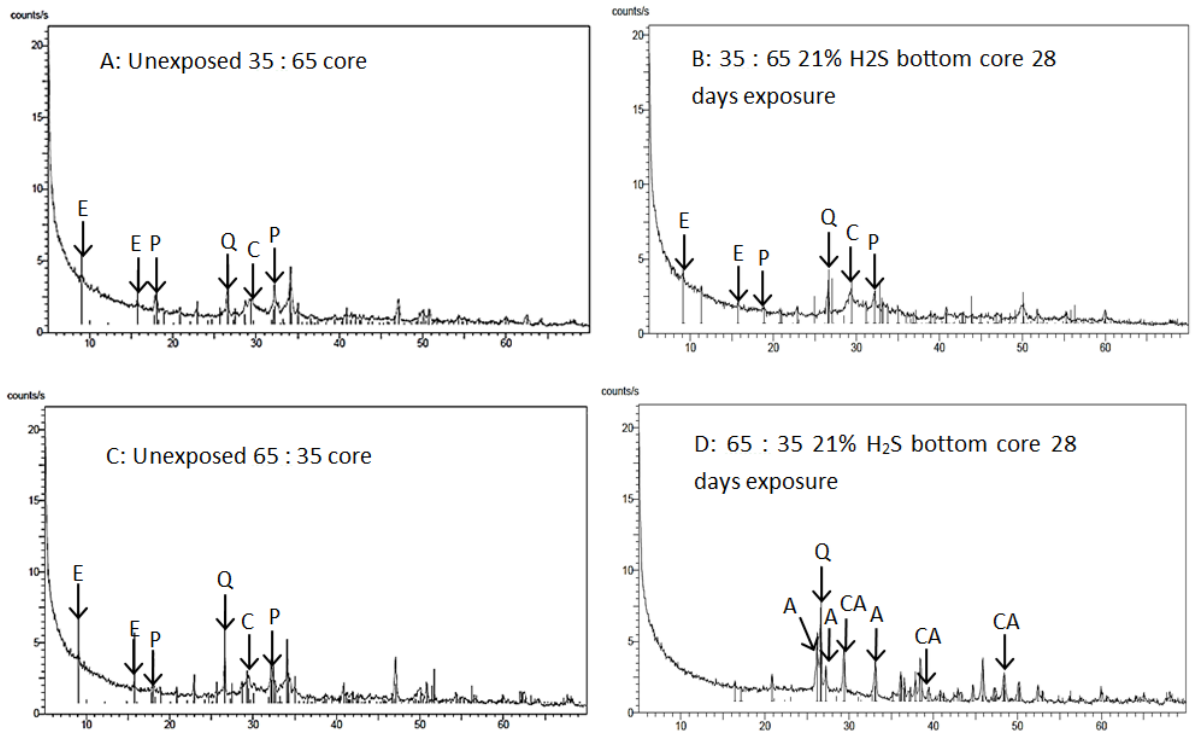

Figure 8: Qualitative XRD analysis results of the interior regions of unexposed 35:65 sample (A), 35:65 sample exposed to 21 mol% H_2S for 28 days, bottom portion (B), unexposed 65:35 sample (C), and 65:35 sample exposed to 21 mol% H_2S for 28 days, bottom portion (D). E = peaks of ettringite; P = peaks of portlandite; Q = peaks of quartz; C = peaks of Ca_3SiO_5; A = peaks of aragonite; CA = peaks of calcite.

Table 3 summarizes the evolution of weight percentages of all mineral phases in the interface region of the pozzolan-amended cement samples as a result of CO_2 and H_2S attack. Analyzed were 65:35 samples exposed to a 1% NaCl brine in contact with a supercritical mixture of CO_2 and 21 mol% H_2S from 2.5 days of exposure to 90 days of exposure (bottom portion). It can be seen that after 2.5 days of exposure, some minerals that were present in the unexposed sample (e.g., brownmillerite, Ca_3SiO_5, Ca_2SiO_4 and ettringite) were transformed into other minerals (e.g., calcite and aragonite). The calcite wt% in the interface region increased from below detection limit (the unexposed sample) to 19% after 90 days of exposure. The aragonite wt% in the interface region increased from below detection limit (the unexposed sample) to 6.8% after 90 days of exposure. The amorphous phase wt% decreased from 82% (unexposed) to 64% (90 days of exposure), which is attributed to the transformation of amorphous C-S-H to calcite and aragonite.

Table 3: Weight percentages of mineral phases in the interface region of the 65:35 samples (bottom portion) exposed to acid gas with 21 mol% H_2S for different durations (2.5 days of exposure to 90 days of exposure) obtained from quantitative XRD analysis

Exposure time (days)	0	2.5	9	28	90
Aragonite	ND	8.3	1.2	8.8	6.8
Brownmillerite	1.8	ND	ND	ND	ND
Calcite	ND	14.9	18.9	18.4	19.0
C3S	5.9	ND	ND	ND	ND
C2S	1.9	ND	ND	ND	ND
Ettringite	2.8	ND	ND	ND	ND
Hematite	ND	ND	ND	ND	ND
Mullite	1.0	ND	ND	ND	ND
Quartz	4.8	6.4	5.3	7.9	10.0
Pyrite	ND	ND	ND	1.0	ND
Crystalline phase total	18.2	29.6	25.4	36.1	35.8
Amorphous phase total	81.8	70.4	74.6	63.9	64.2

3.4 RESULTS OF MICROHARDNESS TESTING

Figure 9 shows the microhardness test results for the bottom portion samples, both at 35:65 and 65:35 compositions, from 0 day of exposure to 90 days of exposure. It can be seen that the microhardness values of the 35:65 samples in the interior region was much lower than those of the 35:65 samples in the interface region, which is due to the formation of carbonate species in the interface region, but not in the interior region. Unlike the 35:65 sample, CO_2 was able to penetrate to the interior region of the 65:35 sample after 2.5 days of exposure, and carbonate species formed in both the interface and interior regions of the 65:35 sample. For this reason, with the exception of the sample exposed for only 2.5 days, the microhardness values of the 65:35 samples in the interior region were very close to those of the 65:35 samples in the interface region.

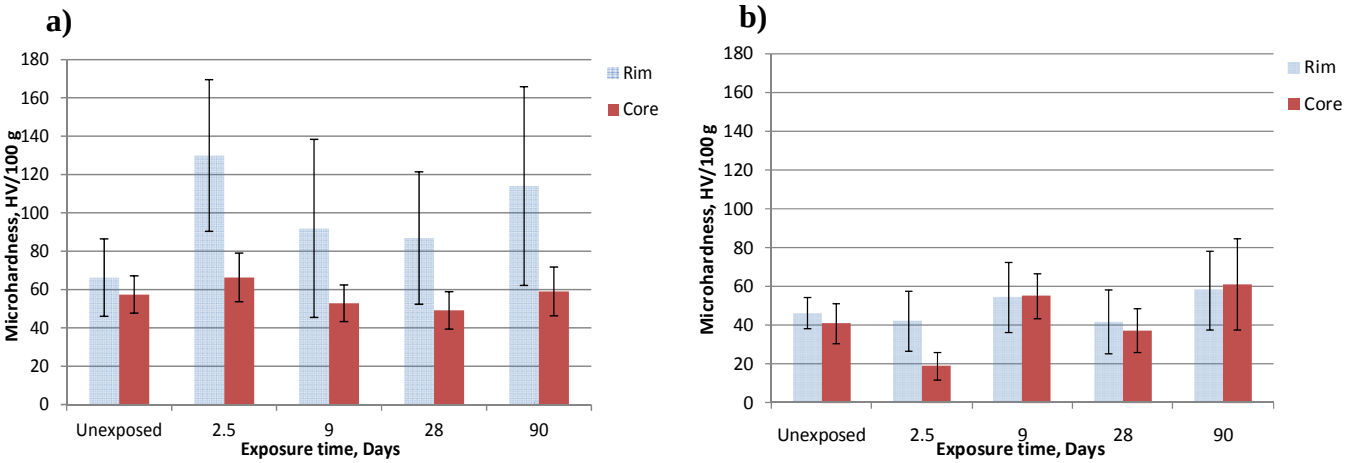

Figure 9: Microhardness test results of interface and core regions of 35:65 samples (a), and interface and core regions of 65:35 samples (b). All the samples tested were bottom portion samples.

3.5 DETERMINATION OF CO_2 AND H_2S ALTERATION RATES BASED ON SEM-BSE AND SEM-EDS ANALYSES

Table 4 shows a summary of locations of carbonate alteration frontier and thicknesses of the sulfur-rich zone in the 35:65 samples exposed for 2.5, 9, 28 and 90 days to a 1 wt % NaCl solution in equilibrium with a supercritical mixture of CO_2 and H_2S (bottom portion). It can be seen that the sulfur-rich zone thickness of the 35:65 samples increased with the increase of exposure time. Different from sulfur-rich zone thickness, the locations of carbonate alteration frontier of samples exposed for 2.5, 9 and 28 days were of similar magnitude, while the location of carbonate alteration frontier exhibited apparent decrease when the exposure time reached 90 days. The shift in the location of carbonate alteration frontier for the 90-day sample is likely attributed to precipitation of more carbonate closer to the interface given the long time of exposure. Adsorption of H_2S on surfaces of cementitious materials may also hinder the advancement of carbonate alteration frontier since the occupation of H_2S on surfaces of cementitious materials prevents contact between CO_2 and cementitious materials, reducing the chance of interaction between CO_2 and cementitious materials.

Table 4: Summary of locations of carbonate alteration frontier and sulfur-rich zone thickness values of 35:65 samples exposed to a saturated H_2S-CO_2 brine of 1 wt% NaCl (bottom portion) from 2.5 days to 90 days

Sample	Location of carbonate alteration frontier(1) (mm)	Sulfur-rich zone thickness(2) (mm)
35:65, 2.5 days of exposure	0.42 ± 0.04	0.23 ± 0.02
35:65, 9 days of exposure	0.44 ± 0.06	0.26 ± 0.04
35:65, 28 days of exposure	0.46 ± 0.04	0.35 ± 0.02
35:65, 90 days of exposure	0.30 ± 0.04	0.39 ± 0.07

(1) Based on SEM-BSE observations of calcite-rich layer
(2) Based on SEM-EDS mapping of elemental sulfur

Figure 10 shows sulfur alteration indices in the interface region, interior region, and the entire cross-section of the samples. The sulfur alteration indices derived from data at both the interface and interior regions were used in combination (e.g., all the 10 data points at the interface region and the 10 data points at the interior region were used together in Equation 1, i.e., $N = 20$) to calculate the degree of sulfur alteration for the entire cross-sections. It can be seen that the interface regions of all samples were significantly altered by H_2S after a short time of exposure.

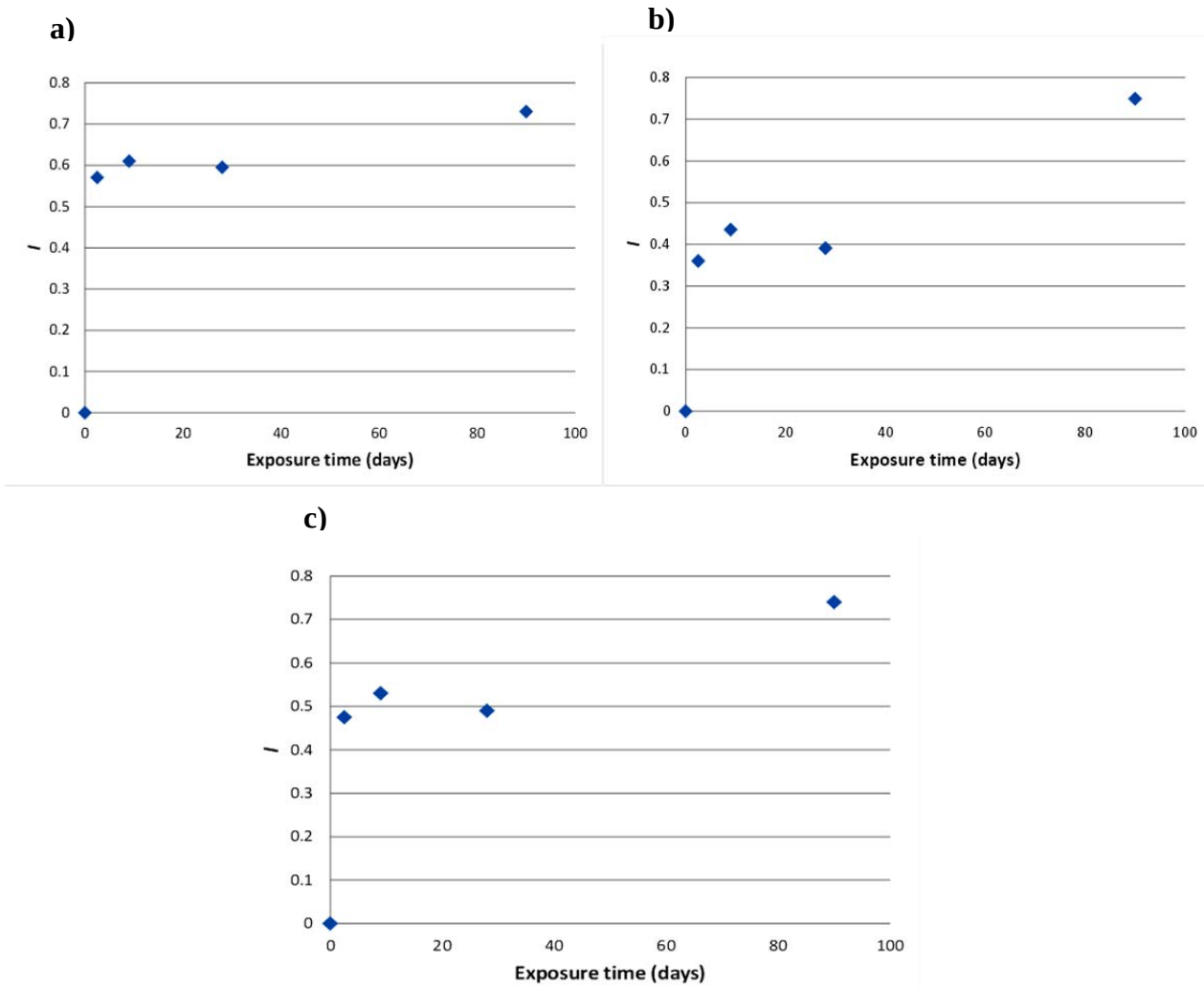

Figure 10: Sulfur alteration indices of 35:65 samples exposed to 1 wt% NaCl solution saturated with CO_2 and H_2S (bottom portion) for different durations in the interface region (10-a), core region (10-b), and the entire cross-section (10-c).

The interior regions of all samples tested were also altered by H_2S, but the degree of alteration was lower than in the interface region. Sulfur alteration indices for the entire cross-sections of samples show that the degree of sulfur alteration increased as exposure time increased, except for the sample exposed for 28 days. The slight decrease of sulfur alteration index from 9 days of exposure to 28 days of exposure might be attributed to measurement error, and more testing is

needed to investigate the change in sulfur alteration index from 9 days of exposure to 28 days of exposure. Compared with the 35:65 sample, H_2S penetrated faster in the 65:35 sample, which can be seen from a higher sulfur alteration index in the interior region of the 65:35 sample (Figure 11).

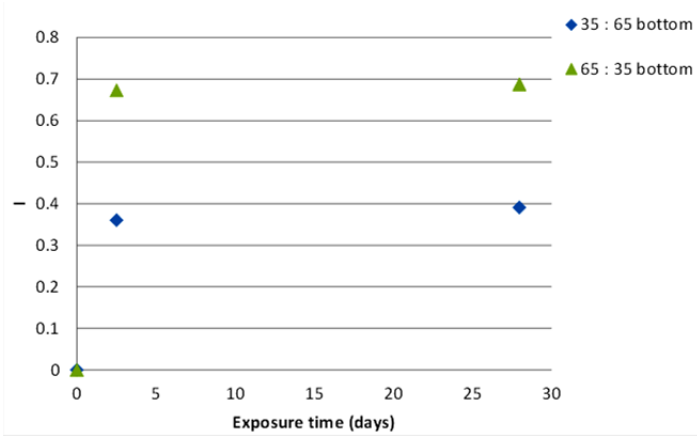

Figure 11: Comparison between sulfur alteration indices at interior regions of 35:65 samples and 65:35 samples. Exposure periods: 0 day, 2.5 days, and 28 days.

Table 5 summarizes the rates of CO_2 and H_2S alteration calculated from the locations of the carbonate alteration frontier, the sulfur-rich zone thicknesses, and the sulfur alteration indices for bottom portion samples. The rate of CO_2 alteration (in units of mm/day) was calculated by:

$$CO_2Rate_{j\ to\ i} = \frac{l_i - l_j}{i - j} \tag{9}$$

where CO_2 $Rate_{j\ to\ i}$ is the average rate of CO_2 alteration during the exposure period of j to i days, l_i is the location of carbonate alteration frontier after i days of exposure, and l_j is the location of carbonate alteration frontier after j days of exposure. In Table 5, if l_i is lower than l_j, then the rate value is marked as "not available", as it is not appropriate to express the rate of CO_2 alteration as a negative value.

Table 5: Rates of CO_2 and H_2S alteration (35:65 samples exposed from 2.5 days to 90 days, bottom portion)

Exposure duration (days)	Rate of CO_2 alteration, mm/day (calculated from the locations of carbonate alteration frontier)	Rate of H_2S alteration, mm/day (calculated from the S-rich zone thicknesses)	Rate of H_2S alteration, day^{-1} (calculated from sulfur alteration indices)
0 to 2.5	0.17	0.09	0.19
2.5 to 9	3.1×10^{-3}	4.6×10^{-3}	7.7×10^{-3}
9 to 28	1.1×10^{-3}	4.7×10^{-3}	not available
28 to 90	not available	6.5×10^{-4}	4.0×10^{-3}

The rate of H_2S alteration derived from sulfur-rich zone (SRZ) thickness data (in units of mm/day) was calculated by:

$$H_2S\ SRZ\ Rate_{j\ to\ i} = \frac{L_i - L_j}{i - j} \tag{10}$$

where $H_2S\ SRZ\ Rate_{j\ to\ i}$ is the average rate of H_2S alteration during the exposure period of j to i days, L_i is the sulfur-rich zone thickness after i days of exposure, and L_j is the sulfur-rich zone thickness after j days of exposure. In Table 5, if L_i is lower than L_j, then the rate value is marked as "not available", as it is not appropriate to express the rate of H_2S alteration as a negative value.

The rate of H_2S alteration derived from sulfur alteration index (I) data, i.e., the H_2S I Rate (in units of day^{-1}) was calculated by:

$$H_2S\ I\ Rate_{j\ to\ i} = \frac{I_i - I_j}{i - j} \tag{11}$$

where $H_2S\ I\ Rate_{j\ to\ i}$ is the average rate of H_2S alteration during the exposure period of j to i days, I_i is the sulfur alteration index after i days of exposure, and I_j is the sulfur alteration index after j days of exposure. In Table 5, if I_i is lower than I_j, then the rate value is marked as "not available", as it is not appropriate to express the rate of H_2S alteration as a negative value.

Table 5 shows that the rates of CO_2 and H_2S alteration decreased as the increase of exposure time, and the advancement of both carbon alteration layer and sulfur-rich zone was significantly slower after 2.5 days of exposure.

3.6 RESULTS OF REACTIVE TRANSPORT MODELING

Figure 12 shows the calcite vol% results of the 35:65 sample obtained from model simulation. The calcite vol% results were validated by a comparison to the observed location of the calcite-rich layer obtained from SEM-BSE imaging. It is important to note that to model the data following 90 days of exposure (Figure 12c), the T value in Equation 4 in the simulation domain of 0 mm to 0.5 mm was reduced from 0.004 to 0.0001. This reduction of T value (corresponding to an increase in tortuosity) is consistent with experimental observation (Arnold et al., 2010), which showed that the formation of calcite in a cement mortar increased the tortuosity of the calcite-rich zone.

The calcite vol% results of the 2.5-day sample and 28-day sample, Figures 12(a) and 12(b), were consistent with SEM-BSE imaging data. For the calcite vol% result of the 90-day sample, as shown in Figure 12(c), the calcite peak predicted by the model was at 0.4 mm, while the calcite-rich zone obtained from SEM-BSE imaging was between 0.2 mm and 0.3 mm. Simulation results show that the calcite-rich layer built up rapidly after a relatively short time of exposure (the peak calcite vol% increased from 5.5% after 2.5 days of exposure to 42% after 28 days of exposure). Further movement of calcite-rich layer to the interior from 28 days of exposure to 90 days of exposure was suppressed, which can be attributed to clogging of pore spaces by calcite and subsequent increase in tortuosity and blockage of CO_2 penetration to the interior.

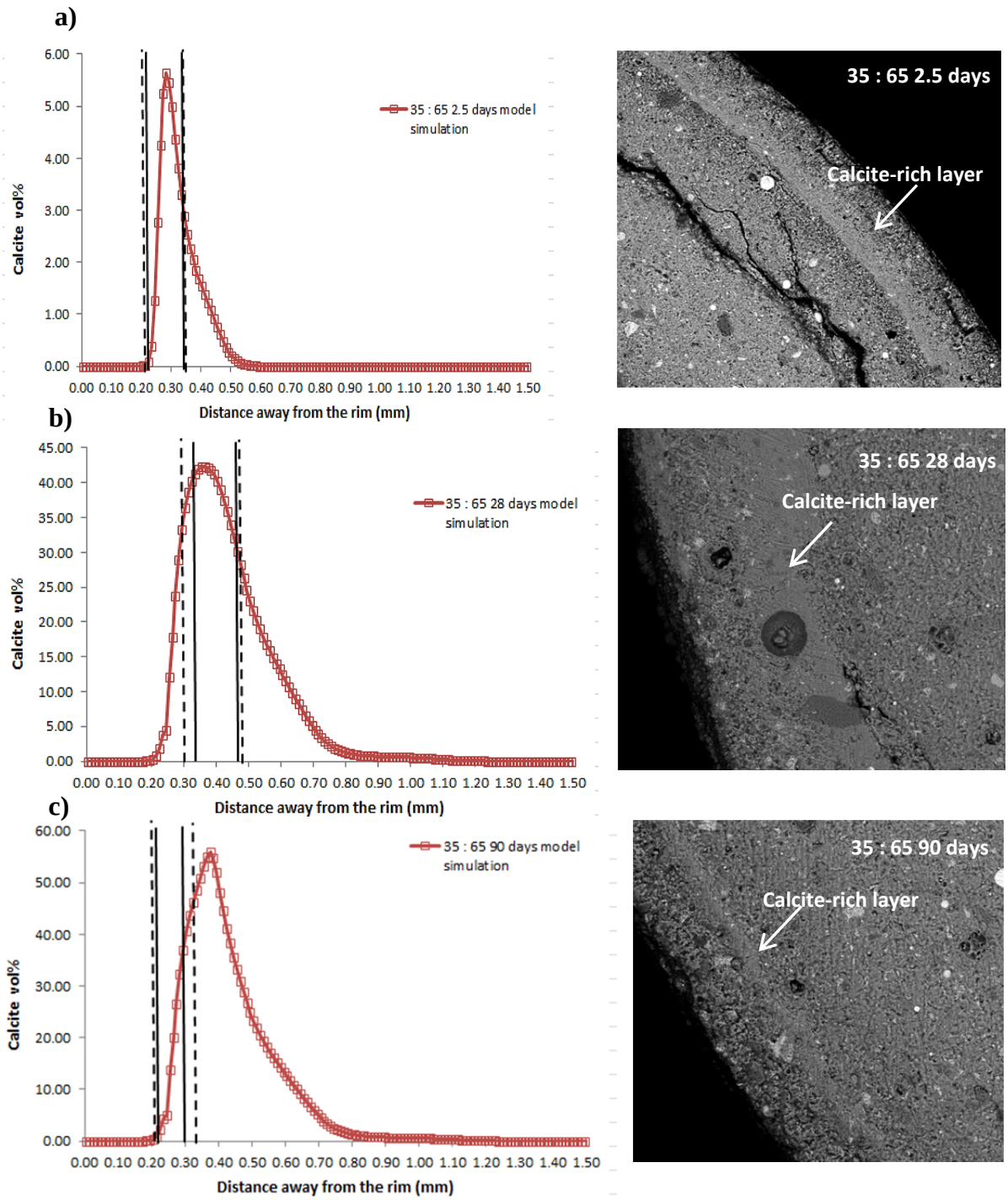

Figure 12: Comparison between calcite volume % model simulation results and calcite-rich layer location data obtained from SEM-BSE images: a) 2.5 days of exposure; b) 28 days of exposure; c) 90 days of exposure. During the model simulation, *T* value was reduced from 0.004 to 0.0001 from 28 days of exposure to 90 days of exposure, so as to reflect the increase in tortuosity. Black lines represent boundaries of the calcite-rich layer in SEM-BSE images, and black dashed lines represent the uncertainties of location measurement of the calcite-rich layer. Details can be seen in Zhang, 2013. Sample: 35:65 sample exposed to 1 wt% NaCl solution saturated with 79 mol% CO_2 and 21 mol% H_2S (bottom portion).

Figure 13 shows the porosity simulation results for the 35:65 sample from 2.5 days of exposure to 30 years of exposure. For the 35:65 sample, an increase in porosity only occurred in the interface region (up to 2 mm away from the surface), even when the exposure time was very long (e.g., 30 years). Though no mechanical strength analysis was conducted in this study, it is not expected that this alteration would lead to a reduction in the mechanical strength of the cement since the alteration only occurred in a narrow region close to the surface of the sample, even after 30 years of exposure. However, further study would be needed to confirm this. All porosity plots had a region with very high porosity adjacent to the interface, which was attributed to the dissolution of calcite close to the interface. The next region in from this region of calcite dissolution had a very low porosity, which was attributed to precipitation of calcite. Continuing towards the casing, beyond this calcite-rich layer, there is another increase in porosity that is also attributed to the dissolution of Ca-bearing minerals.

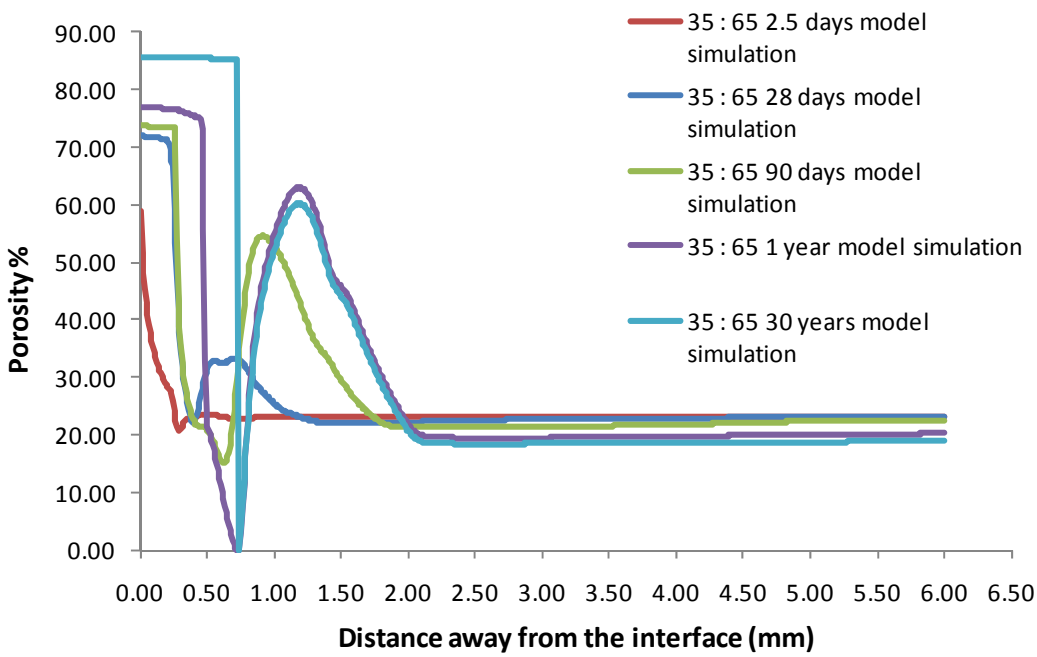

Figure 13: Porosity changes from the interface region to the interior of the 35:65 sample after 2.5 days, 28 days, 90 days, 1 year, and 30 years of exposure.

Based on porosity results in Figure 14 and using Equations 7 and 8 the vertical effective permeability change was calculated and is shown in Figure 15. It can be seen that there was a rapid increase (several orders of magnitude) in effective vertical permeability within 30 days of exposure, followed by much slower increase at longer exposure times. After 30 years of exposure, the effective vertical permeability of the sample increased by 2.3×10^5 times.

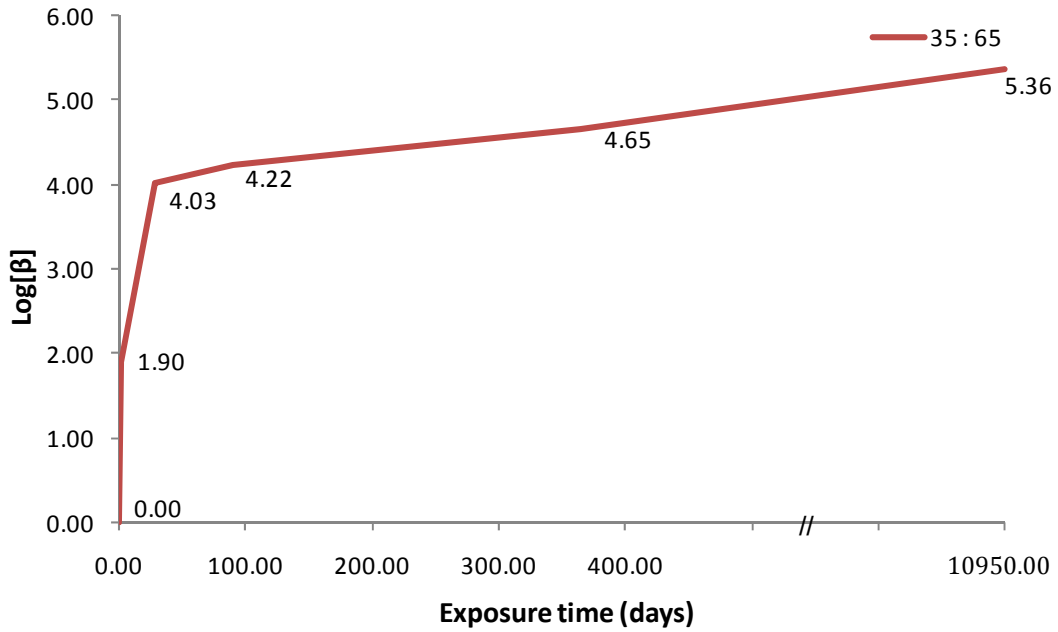

Figure 14: Change in effective vertical permeability of the 35:65 sample from 0 to 10,950 days (30 years) of exposure.

4. DISCUSSION

Optical microscopy analysis, SEM-BSE analysis and SEM-EDS analysis revealed that the interface regions of both the 35:65 and 65:35 samples were altered as a result of CO_2 and H_2S attack at the exposure conditions examined in this study (Table 1). In optical microscopy images, a sheath with a dark color can be distinguished at the outer rim of the sample in comparison to the inner, unaltered zone in the 35:65 sample; the entire 65:35 sample appears impacted as compared to the unexposed sample.

Optical microscopy, SEM coupled with EDS, and qualitative XRD analysis also revealed that compared with the 65:35 sample, the 35:65 sample exhibited slower CO_2 and H_2S penetration to the interior region given the same exposure conditions. The carbonate species were only observed in the interface region of the 35:65 sample after 28 days of exposure, and the sulfur alteration index in the interior region of the 35:65 sample (0.39 after 28 days of exposure, Figure 11) was lower than that of 65:35 sample (0.69 after 28 days of exposure, Figure 11). It is important to note that based on the sulfur alteration index results, H_2S penetrated to the interior region of both 35:65 sample and 65:35 sample after 28 days of exposure. Similar to our findings for 35:65 cement, Kutchko et al. (2011) found evidence of reaction between H_2S and neat cement occurring throughout their sample, whereas evidence of reaction between CO_2 and neat cement occurred only in the interface region.

The reduced CO_2 and H_2S penetrations in the 35:65 sample are explained primarily by the formation of a calcite-rich layer in the interface region of the 35:65 sample. The formation of a calcite-rich layer in the interface region inhibits penetration of CO_2 and H_2S across the layer. As there was no calcite-rich layer in the interface region of the 65:35 sample, penetration of CO_2 and H_2S to the interior region was not hindered. Another reason for the difference in acid gas penetration rate to the interior regions of these samples is that the 65:35 sample contained a much higher amount of fly ash particles than did the 35:65 sample. There is no binding phase between fly ash particles, thus more pore space exists in the fly ash-rich samples (Uygunoglu et al., 2012). As a result, the more porous 65:35 sample favored the penetration of CO_2 and H_2S to the interior region. In addition, as compared with the 35:65 sample, the 65:35 sample had a lower slurry density and higher water to cement ratio (Kutchko et al., 2009), which results in a higher permeability of the 65:35 sample.

Though both the interface region and the interior region of the 65:35 sample were altered by CO_2 and H_2S attack after short exposure duration, the microhardness test results showed that the alteration induced by CO_2 and H_2S may not lead to mechanical strength loss. This is due to the formation of carbonate species in the interior region. For example, the microhardness of the 65:35 sample in the interior region after 90 days of exposure was even higher than that of unexposed 65:35 sample. In comparison, the microhardness in the interior region of the 35:65 sample after 90 days of exposure was very close to that of unexposed sample. More research is needed to correlate these microhardness values with the macro-scale mechanical strength of the samples.

The interaction between H_2S and pozzolan-amended cement is explained as H_2S-derived SO_4^{2-} attack, which has been discussed in previous studies (Tixier, 2000; Santhanam et al., 2001; Kutchko et al., 2011). The first step of the mechanism is the formation of SO_4^{2-} from the oxidation of H_2S. In pozzolan-amended cement, the main oxidants are Fe(III)-bearing minerals. The second step of the mechanism is the interaction between SO_4^{2-}, Ca^{2+}, Al-bearing ions and

water to produce ettringite. Compared with the original mineral phases in pozzolan-amended cement, ettringite is an expansive material, the formation of which may cause integrity loss of the cement under unconfined conditions. However, the integrity loss was not observed in this research and may not be observed in the field where confining pressures are present. In the last step, Fe^{2+} produced from the H_2S oxidation reaction reacts to produce pyrite. Under the exposure conditions of this study, there was negligible oxygen present and the only phases that could oxidize H_2S to SO_4^{2-} during exposure were the Fe(III)-bearing phases in pozzolan-amended cement. Therefore, it would appear that the degree of H_2S-derived SO_4^{2-} attack depends on the availability of Fe(III)-bearing phases in the cement. Fe (III)-bearing phases are not evenly distributed throughout the pozzolan-amended cement. Most Fe (III)-bearing phases aggregate in iron-rich particles (Fe wt% of the iron-rich particles is 42% from SEM-EDS analysis) from the fly ash additive, and the Fe wt% in the cement matrix is 3%. As a result, the products of H_2S interacting with pozzolan constituents in amended cement are ettringite and pyrite, mainly formed in the regions with Fe-rich particles (details can be seen in Zhang, 2013). However, as Fe (III)-bearing phases are minor phases in pozzolan-amended cement, the formation of ettringite and pyrite is limited, and does not contribute significantly to the porosity and permeability changes of pozzolan-amended cement.

Though formation of ettringite and pyrite does not contribute much to changes in porosity and permeability, an increase in the H_2S content of the acid gas is predicted to enhance the dissolution of Ca-bearing minerals in pozzolan-amended cement, which results in the formation of more calcite. Those processes increase the porosity of the Ca-bearing mineral dissolution layer and reduce the porosity of the calcite-rich layer (Figure 15). The enhancement of the dissolution of Ca-bearing minerals is mainly due to an increase in the supply of H^+ due to the presence of more dissolved H_2S.

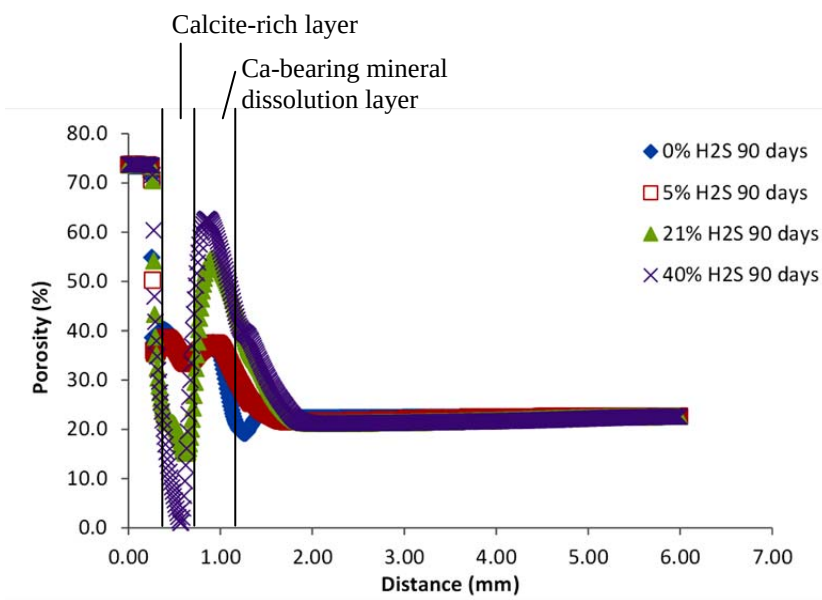

Figure 15: Predicted effect of H_2S mol% in acid gas on porosity change of pozzolan-amended cement (35:65 sample).

The reactive transport model predicts the formation of a calcite-rich layer close to the surface of the 35:65 sample after 2.5 days of exposure, and the calcite vol% in the calcite-rich layer increases significantly after 28 days of exposure. This prediction is consistent with observations obtained from SEM-BSE. Formation of a calcite-rich layer is believed to reduce the porosity of the cement and contribute to its "self-sealing" (Kutchko et al., 2007; Carey et al., 2010). However, Barlet-Gouédard et al. (2007), Fabbri et al. (2009), and Gherardi et al. (2012) reported that formation of cracks and significant strength loss were usually recognized in association with extensive carbonation processes. In the modeling performed in this study, the extensive carbonation at the surface of the pozzolan-amended cement occurred rapidly, which could lead to crack formation and strength loss of the pozzolan-amended cement.

Dissolution of Ca-bearing cement materials is the main source of Ca^{2+} to form calcite. For pozzolan-amended cement, the modeling indicated that C-S-H, C3S and $Ca(OH)_2$ were the three minerals that provided most of the free Ca^{2+} in the system. C-S-H was the most important Ca^{2+} source from 2.5 days to 90 days of exposure; C3S was also an important Ca^{2+} source when the exposure time was short (2.5 days). When the exposure time became long (e.g., 90 days), all of the C3S in the 35:65 sample was dissolved and did not contribute to the production of Ca^{2+} (Zhang, 2013).

There was a significant increase in effective vertical permeability of the sample after 2.5 days of exposure due to re-dissolution of calcite in the region close to the interface. After 30 years of exposure, the effective vertical permeability was predicted to increase by 2.3×10^5 times. It is important to note that the model successfully predicted an increase in porosity and vertical permeability at the interface region of cement due to the re-dissolution of calcite, which has been observed experimentally (Duguid et al., 2005; Kutchko et al., 2007). However, this porosity increase due to calcite re-dissolution may not occur at a high rate at real storage sites, because of the capacity of reservoir rocks to buffer the pH of CO_2-rich reservoir pore water to values around 5 (Gherardi et al., 2012). That is to say, the model may overestimate the increase in permeability of wellbore cement in real caprock-cement-brine systems.

5. CONCLUSIONS

In this research, pozzolan-amended cement samples (35:65 and 65:35 samples) were exposed to CO_2 and H_2S under typical carbon storage conditions, and SEM-BSE, SEM-EDS, XRD and microhardness analyses were applied to characterize the samples following exposure. Reactive transport modeling was used to help interpret the experimental data and to predict the changes in physical and chemical properties of pozzolan-amended wellbore cement for longer exposure times.

This research suggests that the 35:65 sample was more resistant to CO_2 and H_2S attack than the 65:35 sample under the same exposure conditions. Quantification of alteration rates indicated that for the 35:65 sample (bottom portion), significant alteration only occurred at the surface of the sample after 90 days of exposure, and the alteration rates were only 3.3×10^{-3} mm/day for CO_2 and 4.3×10^{-3} mm/day for H_2S. For the 65:35 sample (bottom portion), the alteration rate could not be calculated, as the calcite-rich layer and sulfur-rich zone were not clear in SEM-BSE and SEM-EDS images for the 65:35 sample. However, it was observed that both CO_2 and H_2S were able to penetrate to the interior of the 65:35 sample after 2.5 days of exposure. The higher penetration rates of CO_2 and H_2S in the 65:35 sample could be attributed to the higher porosity and lower tortuosity of the 65 vol% pozzolan : 35 vol% cement sample.

The microhardness testing results indicate that significant loss of microhardness did not occur at either the interface or the interior regions of the samples after 90 days of exposure for both 35:65 and 65:35 cement samples. Therefore, though the interior region of the 65 vol% pozzolan : 35 vol% cement sample was altered by CO_2 and H_2S after 2.5 days of exposure, the data suggest that this alteration may not lead to a loss in mechanical strength, although such a hypothesis requires further investigation.

The reactive transport model developed in this research was able to model the significant alteration at the surface of the 35:65 sample. The solid phase calcite vol% results produced by the model were consistent with SEM-BSE data. Due to the significant alteration in the surface region of the samples, the model predicted a 2.3×10^{5} times increase in effective vertical permeability of the cement after 30 years of exposure. Though significant increase in effective vertical permeability of 35 vol% pozzolan : 65 vol% cement sample in contact with CO_2 and H_2S-saturated brine was observed, this increase does not necessarily suggest that there would be a leakage of acid gas to shallow groundwater during acid gas co-storage, since only the bottom portion of a well is in contact with the brine, and the other portions of a well that are not directly in contact with the brine are expected to have much lower increase in vertical permeability, if any. Therefore, more investigations are needed to correlate the effective permeability change of the wellbore cement in contact with brine with the effective permeability change of the wellbore cement along the entire length of a well.

Based on the results obtained in this research, some future work would be useful in further understanding the full impact of cement corrosion on the risk associated with co-storage sites. Suggestions for future work are listed below.

First, there is a need to correlate chemical reactions and porosity/permeability evolution with mechanical strength change of pozzolan-amended cement. This research used microhardness testing as an approach to quantify mechanical strength of the sample, but the microhardness test results only represent mechanical strength at a micro-scale, which does not reflect the macro-

scale mechanical strength of the sample. Therefore, there is a need to find an appropriate method to quantify macro-scale mechanical strength, and correlate that with chemical reactions and porosity/permeability evolution of pozzolan-amended cement.

Second, there is a need to find an experimental approach to validate porosity and permeability results obtained from model simulation. Permeability measurement of cement cores under reservoir conditions (pressure and temperature) is possible using the core flow testing equipment at NETL. Within limits, porosity can be measured via optical microscopy.

Third, there is a need to obtain field cement samples at acid gas storage sites and compare the actual field samples with the laboratory-exposed samples of this study. There have been several acid gas injection sites in Canada (e.g., Fort Nelson acid gas injection site in British Columbia, Canada), and it may be possible to acquire field samples of exposed cement from these sites for characterization. The characterization of these samples will permit the field validation of the research results, including the surface alteration and penetration estimates over time.

Finally, there is a need to improve the reactive transport model developed in this research, so as to make the model capable of dealing with more complicated scenarios. To be specific, the current model is only for no-flow, diffusion-controlled transport conditions. The model can be improved to deal with scenarios involving convective flow, which may occur in the cement after porosity and permeability changes. Moreover, the model can be upgraded to a large-scale 2-D model, so as to simulate the entire wellbore cement-caprock-brine system. The model can also include multi-phase flows (e.g., brine saturated with CO_2 and H_2S, and supercritical CO_2-H_2S), and set up direct reactions between wellbore cement and CO_2-H_2S supercritical fluid.

6. REFERENCES

Alberta Geological Survey. Deep Injection of Acid Gas (H_2S) in Western Canada, 2009. http://www.ags.gov.ab.ca/co2_h2s/co2_acidgas.html (accessed: March 2013).

American Petroleum Institute. *API Recommended Practice 10B: Recommended Practice for Testing Well Cements*; API: Washington, DC, 1997.

American Petroleum Institute. *Worldwide Cementing Practices*; API: Dallas, TX, 1991.

Arnold, J.; Meeussen, J.; Garrabrants, A.; van der Sloot, H. A.; Kosson, D. S. The Impact of Mineral Deposition by Carbonation and Dissolution on Leaching of Constituents from a Cement Mortar. In *2010 WM Symposia*; Phoenix, AZ, 2010.

Barlet-Gouédard, V.; Rimmelé, G.; Goffé, B.; Porcherie, O. Well technologies for CO_2 geological storage: CO_2-resistant cement. *Oil Gas Sci. Technol.* **2007,** *62*, 325–334.

Barlet-Gouédard, V.; Rimmelé, G.; Porcherie, O.; Quisel, N.; Desroches, J. A solution against well cement degradation under CO_2 geological storage environment. *Int. J. Greenhouse Gas Control* **2009,** *3*, 206–216.

Bijen, J. Benefits of slag and fly ash. *Constr. Build. Mater.* **1996,** *10*, 309–314.

Brandvoll, Ø.; Regnault, O.; Munz, I. A.; Iden, I. K.; Johansen, H. Fluid–solid interactions related to subsurface storage of CO_2 Experimental tests of well cement. *Energy Procedia* **2009,** *1*, 3367–3374.

Brunet, J. L.; Li, L.; Karpyn, Z. T.; Kutchko, B. G.; Strazisar, B. R.; Bromhal, G. Dynamic evolution of cement composition and transport properties under conditions relevant to geological carbon sequestration. *Energy & Fuels* **2013,** *27*, 4208–4220.

Canpolat, F.; Yılmaz, K.; Kösec, M. M.; Sümer, M.; Yurdusev, M. A. Use of zeolite, coal bottom ash and fly ash as replacement materials in cement production. *Cem. Concr. Res.* **2004,** *34*, 731–735.

Carey, J. W.; Svec, R.; Grigg, R.; Zhang, J.; Crow, W. Experimental investigation of wellbore integrity and CO_2–brine flow along the casing–cement microannulus. *Int. J. Greenhouse Gas Control* **2010,** *4*, 272–282.

Carey, J. W.; Wigand, M.; Chipera, S. J.; Woldegabriel, G.; Pawar, R.; Lichtner, P. C.; Wehner, S. C.; Raines, M. A.; Guthrie, G. D. Analysis and performance of oil well cement with 30 years of CO_2 exposure from the SACROC Unit, West Texas, USA. *Int. J. Greenhouse Gas Control* **2007,** *1*, 75–85.

Carroll, J. J. *Acid Gas Injection and Carbon Dioxide Sequestration*; John Wiley and Sons: Hoboken, NJ, 2010.

Craft, B. C.; Hawkins, M. F.; Terry, R. E. *Applied Petroleum Reservoir Engineering*; Prentice Hall: Englewood Cliffs, NJ, 1991; p 431.

Duguid A.; Radonjic M.; Scherer G. Degradation of well cement exposed to carbonated brine. In *Proceedings of the 4th Annual Conference on Carbon Capture and Sequestration*, Alexandria, VA, May 2–5, 2005.

Duguid, A.; Radonjic, M.; Bruant, R.; Mandecki, T.; Scherer, G.; Celia, M. The effect of CO_2 sequestration on oil well cements. In *Proceedings of the 7th Annual Conference on Greenhouse Gas Control Technologies*, Vancouver, Canada, Sept 5–9, 2004.

Fabbri, A.; Corvisier, J.; Schnubel, A.; Brunet, F.; Goffé, B.; Rimmelé, G.; Barlet-Gouédard, V. Effect of carbonation on the hydro-mechanical properties of Portland cements. *Cem. Concr. Res.* **2009,** *39*, 1156–1163.

Fabbri, A.; Jacquemet, N.; Seyedi, D. M. A chemo-poromechanical model of oilwell cement carbonation under CO_2 geological storage conditions. *Cem. Concr. Res.* **2012,** *42*, 8–19.

Ghabezloo, S.; Sulem, J.; Saint-Marc, J. Evaluation of a permeability‐porosity relationship in a low-permeability creeping material using a single transient test. *Int. J. Rock Mech. Min. Sci.* **2009,** *46*, 761–768.

Gherardi, F.; Pascal Audigane, P.; Gaucher, E. C. Predicting long-term geochemical alteration of wellbore cement in a generic geological CO_2 confinement site: Tackling a difficult reactive transport modeling challenge. *J. Hydrol.* **2012,** *420–421*, 340–359.

Gibbins, J.; Chalmers, H. Carbon capture and storage. *Energy Policy* **2008,** *36*, 4317–4322.

Hawthorne, S. B.; Miller, D. J.; Holubnyak, Y.; Harju, J. A.; Kutchko, B. G.; Strazisar, B. R. Experimental investigations of the effects of acid gas (H_2S/CO_2) exposure under geological sequestration conditions. *Energy Procedia* **2011,** *4*, 5259–5266.

Hovorka, S. D. Field Experiment for CO_2 Sequestration–Update on the Frio Brine Pilot Experiment—six months after injection. Bureau of Economic Geology, TX, 2005. http://www.beg.utexas.edu/environqlty/co2seq/fieldexperiment.htm (accessed Mar 2013).

Huet, B. M.; Prevost, J. H.; Scherer, G. W. Quantitative reactive transport modeling of Portland cement in CO_2-saturated water. *Int. J. Greenhouse Gas Control* **2010,** *4*, 561–574.

Jacquemet, N.; Pironon, J.; Lagneau, V.; Saint-Marc, J. Armouring of well cement in H_2S-CO_2 saturated brine by calcite coating—Experiments and numerical modeling. *Appl. Geochem.* **2012,** *27*, 782–795.

Jacquemet, N.; Pironon, J.; Saint-Marc, J. Mineralogical changes of a well cement in various H_2S-CO_2 (-brine) fluids at high pressure and temperature. *Environ. Sci. Technol.* **2008,** *42*, 282–288.

Kula, I.; Olgun, A.; Erdogan, Y.; Sevinc, V. Effects of colemanite waste, cool bottom ash, and fly ash on the properties of cement. *Cem. Concr. Res.* **2001,** *31*, 491–494.

Kutchko B. G.; Strazisar B. R.; Hawthorne S. B.; Lopano C. L.; Miller D. J.; Hakala J. A.; Guthrie G. D. H_2S–CO_2 reaction with hydrated Class H well cement: Acid-gas injection and CO_2 Co-sequestration. *Int. J. Greenhouse Gas Control* **2011,** *5*, 880–888.

Kutchko, B. G.; Strazisar, B. R.; Dzombak, D. A.; Lowry, G. V.; Thaulow, N. Degradation of well cement by CO_2 under geologic sequestration conditions. *Environ. Sci. Technol.* **2007,** *41*, 4787–4792.

Kutchko, B. G.; Strazisar, B. R.; Huerta, N.; Lowry, G. V.; Dzombak, D. A.; Thaulow, N. CO_2 Reaction with Hydrated Class H Well Cement under Geologic Sequestration Conditions: Effects of Flyash Admixtures. *Environ. Sci. Technol.* **2009,** *43*, 3947–3952.

Li, L.; Steefel, C. I.; Kowalsky, M. B.; Englert, A.; Hubbard, S. S. Effects of physical and geochemical heterogeneities on mineral transformation and biomass accumulation during biostimulation experiments at Rifle, Colorado. *J. Contam. Hydrol.* **2010,** *112*, 45–63.

Marty, N. C. M.; Tournassat, C.; Burnol, A.; Giffaut, E.; Gaucher, E. C. Influence of reaction kinetics and mesh refinement on the numerical modelling of concrete/clay interactions. *J. Hydrol.* **2009,** *364*, 58–72.

Mason, H. E.; DuFrane, W. L.; Walsh, S.; Dai, Z.; Charnvanichborikarn, S.; Carroll, S. Chemical and mechanical properties of wellbore cement altered by CO_2-rich brine using a multi-analytical approach. *Environ. Sci. Technol.* **2013,** *47*, 1745–1752.

Newell, D. L.; Carey, J. W. Experimental Evaluation of Wellbore Integrity Along the Cement-rock Boundary. *Environ. Sci. Technol.* **2013,** *47*, 276–282.

Rackley, S. A. *Carbon capture and storage*; Elsevier: Burlington, MA, 2010.

Rosenberg, A. Using Fly Ash in Concrete. http://precast.org/2010/05/using-fly-ash-in-concrete/ (accessed Mar 2013).

Santhanam, M.; Mesnashi, D. C.; Olek, J. Sulfate attack research-whither now? *Cem. Concr. Res.* **2001,** *31*, 8845–8851.

Steefel, C. I. *CrunchFlow User's Manual*; Lawrence Berkeley National Laboratory: Berkeley, CA, 2009.

Steefel, C. I.; Lasaga, A. C. A coupled model for transport of multiple chemical species and kinetic precipitation/dissolution reactions with application to reactive flow in single phase hydrothermal systems. *Am. J. Sci.* **1994,** *294*, 529–592.

Tixier, R. Microstructural development and sulfate attack modeling in blended cement-based materials. Ph.D. Dissertation, Arizona State University, Tempe, AZ, 2000.

Uygunoglu, T.; Topcu, I. B.; Gencel, O.; Brostow, W. The effect of fly ash content and types of aggregates on the properties of pre-fabricated concrete interlocking blocks (PCIBs). *Constr. Build. Mater.* **2012,** *30*, 180–187.

Wertz, F.; Gherardi, F.; Blanc, P.; Bader, A. G.; Fabbri, A. Cement CO_2-alteration propagation at the well-caprock-reservoir interface and influence of diffusion. *Int. J. Greenhouse Gas Control* **2013,** *12*, 9–17.

White C. M.; Strazisar B. R.; Granite E. J.; Hoffman J. S.; Pennline, H. W. Separation and capture of CO_2 from large stationary sources and sequestration in geological formations—coalbeds and deep saline aquifers. *J. Air Waste Manage.* **2003,** *53*, 645–715.

Wilke, C. R.; Chang, P. Correlation of Diffusion Coefficients in Dilute Solutions. *AIChE J.* **1955,** *1*, 264–270.

Xu T.; Sonnenthal E.; Spycher N.; Pruess, K. *TOUGHREACT User's Guide: A Simulation Program for Non-Isothermal Multiphase Reactive Geochemical Transport in Variable Saturated Geologic Media (May 24, 2004);* Paper LBNL-55460; Lawrence Berkeley National Laboratory: Berkeley, CA, 2004.

Zhang, M.; Bachu, S. Review of integrity of existing wells in relation to CO_2 geological storage: What do we know? *Int. J. Greenhouse Gas Control* **2011,** *5*, 826–840.

Zhang, L. Acid gas interactions with pozzolan-amended wellbore cement under geologic sequestration conditions. Ph.D. dissertation, Carnegie Mellon University, Pittsburgh, PA, 2013.

Zhang, L.; Dzombak, D. A.; Nakles, D. V.; Hawthorne, S. B.; Miller, D. J.; Kutchko, B. G.; Lopano, C. L.; Brian R. Strazisar, B. R. Rate of H_2S and CO_2 attack on pozzolan-amended Class H well cement under geologic sequestration conditions. *Int. J. Greenhouse Gas Control* **2014,** *27*, 299–308.

NRAP is an initiative within DOE's Office of Fossil Energy and is led by the National Energy Technology Laboratory (NETL). It is a multi-national-lab effort that leverages broad technical capabilities across the DOE complex to develop an integrated science base that can be applied to risk assessment for long-term storage of carbon dioxide (CO_2). NRAP involves five DOE national laboratories: NETL, Lawrence Berkeley National Laboratory (LBNL), Lawrence Livermore National Laboratory (LLNL), Los Alamos National Laboratory (LANL), and Pacific Northwest National Laboratory (PNNL).

Technical Leadership Team

Jens Birkholzer
LBNL Technical Coordinator
Lawrence Berkeley National Laboratory
Berkeley, CA

Grant Bromhal
NETL Technical Coordinator
Lead, Reservoir Performance Working Group
Office of Research and Development
National Energy Technology Laboratory
Morgantown, WV

Chris Brown
PNNL Technical Coordinator
Pacific Northwest National Laboratory
Richmond, WA

Susan Carroll
LLNL Technical Coordinator
Lawrence Livermore National Laboratory
Livermore, CA

Josh White
Lead, Induced Seismicity Working Group
Lawrence Livermore National Laboratory
Livermore, CA

Diana Bacon
Lead, Groundwater Protection Working Group
Pacific Northwest National Laboratory
Richmond, WA

Tom Daley
Lead, Strategic Monitoring Working Group
Lawrence Berkeley National Laboratory
Berkeley, CA

George Guthrie
Technical Director, NRAP
Office of Research and Development
National Energy Technology Laboratory
Pittsburgh, PA

Rajesh Pawar
LANL Technical Coordinator
Lead, Systems/Risk Modeling Working Group
Los Alamos National Laboratory
Los Alamos, NM

Tom Richard
Deputy Technical Director, NRAP
The Pennsylvania State University
NETL-Regional University Alliance
State College, PA

Nik Huerta
Lead, Migration Pathways Working Group
Office of Research and Development
National Energy Technology Laboratory
Albany, OR

Sean Plasynski
Director
Strategic Center for Coal
National Energy Technology Laboratory
U.S. Department of Energy

John Wimer
Director
Office of Coal and Power R&D
National Energy Technology Laboratory
U.S. Department of Energy

Susan Maley
Technology Manager
Crosscutting Research
National Energy Technology Laboratory
U.S. Department of Energy

Mark Ackiewicz
Director
Division of Carbon Capture and Storage
Office of Fossil Energy
U.S. Department of Energy

NRAP Executive Committee

Cynthia Powell
Director
Office of Research and Development
National Energy Technology Laboratory
U.S. Department of Energy

Alain Bonneville
Laboratory Fellow
Pacific Northwest National Laboratory

Donald DePaolo
Chair, NRAP Executive Committee
Associate Laboratory Director
Energy and Environmental Sciences
Lawrence Berkeley National Laboratory

Melissa Fox
Program Manager
Applied Energy Programs
Los Alamos National Laboratory

Roger Aines
Chief Energy Technologist
Lawrence Livermore National
Laboratory

George Guthrie
Technical Director, NRAP
Office of Research and Development
National Energy Technology Laboratory

NRAP Technical Report Series